JOURNAL OF PETROLOGY | VOLUME 46 | NUMBER 3 | PAGES 555–578 | 2005 | doi:10.1093/petrology/egh088

Experimentally Determined Phase Relations in Hydrous Peridotites to 6·5 GPa and their Consequences on the Dynamics of Subduction Zones

P. FUMAGALLI* AND S. POLI

UNIVERSITÀ DEGLI STUDI DI MILANO, DIPARTIMENTO DI SCIENZE DELLA TERRA, VIA BOTTICELLI 23, 20133, MILANO, ITALY

RECEIVED FEBRUARY 29, 2004; ACCEPTED OCTOBER 6, 2004
ADVANCE ACCESS PUBLICATION DECEMBER 3, 2004

Fluid-saturated subsolidus experiments from 2·0 to 6·5 GPa, and from 680 to 800°C have been performed on three model peridotites in the system Na_2O–CaO–FeO–MgO–Al_2O_3–SiO_2–H_2O (NCFMASH). Amphibole and chlorite coexist up to 2·4 GPa, 700°C. Chlorite persists to 4·2 GPa at 680°C. Starting from 4·8 GPa, 680°C a 10 Å phase structure replaces chlorite in all compositions. The 10 Å phase structure contains significant Al_2O_3 (up to 10·53 wt %) deviating from the MgO–SiO_2–H_2O 10 Å phase (MSH 10 Å phase). A mixed layered structure (chlorite–MSH 10 Å phase) is proposed to account for aluminium observed. In the Tinaquillo lherzolite amphibole breakdown occurs via the reaction

$$amphibole + olivine \pm H_2O = clinopyroxene + orthopyroxene + chlorite.$$

Thermal stability of chlorite (chlorite + orthopyroxene = forsterite + garnet + H_2O) is shifted towards lower temperatures, compared with the system MASH. Furthermore, the chlorite thermal breakdown is also related to the degenerate reaction

$$chlorite + clinopyroxene = olivine + garnet(\pm orthopyroxene) + H_2O.$$

Chlorite and the Al-10 Å phase structure contribute significantly to the water budget in subduction zones in the depth range relevant for arc magmatism, whereas amphibole-related fluid release is restricted to the forearc region. Chlorite and Al-10 Å phase breakdowns might explain the occurrence of a double seismic zone by dehydration embrittlement.

KEY WORDS: *amphibole; chlorite; high pressure; peridotites; subduction zones*

INTRODUCTION

Water is transported, released and recycled into the Earth's mantle via subduction processes. Field evidence reveals the occurrence of extensively hydrated peridotites in a variety of oceanic settings, i.e. fast- and slow-spreading ridges (Frueh-Green *et al.*, 1996; Muller *et al.*, 1997) and passive continental margins (Boillot *et al.*, 1988); profound hydrothermal exchange with sea water is expected to occur not only close to ridge segments and along fracture zones (Constantin, 1999) but possibly also in flexural deformation zones at subduction margins (Peacock, 2001). Constraints on the distribution of hydrous phases along the subducting lithosphere and in the overlying mantle wedge are crucial in depicting the dynamic evolution of subduction zones.

Amphibole dehydration in variably enriched ultramafics has long been held responsible for mass-transfer generating arc magmatism (Wyllie, 1988; Davies & Stevenson, 1992; Tatsumi & Eggins, 1995), for seismic properties at the slab–wedge interface, and for variations in buoyancy forces. Current knowledge on amphibole stability in ultramafic compositions mainly relies on near-solidus experiments performed by Green (1973), Mysen & Boettcher (1975), Wallace & Green (1991) and Niida & Green (1999), but amphibole compositional variations and its phase relationships at temperatures below 920°C are substantially unknown.

*Corresponding author. Telephone: +390250315588. Fax: +390250315597. E-mail: Patrizia.Fumagalli@unimi.it

More recently, emphasis has been given to antigorite because of the large amount of H_2O released at its breakdown, its notable abundance in a variety of bulk compositions (including harzburgites), a pressure stability exceeding 5 GPa, and, last but not least, because of the possible relations to the presence of double seismic zones in subducting slabs (Yamasaki & Seno, 2003). A considerable amount of experimental work in the chemical systems $MgO–SiO_2–H_2O$ (MSH) and $MgO–Al_2O_3–SiO_2–H_2O$ (MASH) has been performed to estimate the maximum stability field of antigorite (Ulmer & Trommsdorff, 1995, 1999; Wunder *et al.*, 2001; Bromiley & Pawley, 2003) and to unravel the location of reactions responsible for H_2O transfer from antigorite to dense hydrous magnesium silicates (DHMS) such as Phase A (Kawamoto *et al.*, 1996; Ulmer & Trommsdorff, 1999) or the 10 Å phase (Pawley & Wood, 1995; Fumagalli *et al.*, 2001).

Similarly, at temperatures exceeding antigorite stability, the maximum thermal stability of chlorite, the 10 Å phase, and other DHMS at high pressure have been investigated in the model systems MSH and MASH (Staudigel & Schreyer, 1977; Fockenberg, 1995; Pawley & Wood, 1995; Frost, 1999; Pawley, 2003) with the main purpose of identifying potential H_2O reservoirs for volatile transfer to the deep mantle.

Addition of Fe, Ca and Na, approaching natural bulk compositions involved in subduction processes, results in profound effects on phase equilibria and stabilities. Element partitioning between chlorite, amphibole, garnet, pyroxenes, etc. is expected to modify hydrous phase stability as modelled in very simple chemical systems. As an example, solidus and near-solidus experiments performed on bulk compositions approaching natural variably enriched ultramafic rocks (Wallace & Green, 1991) actually suggest that bulk alkali content strongly influences the amphibole stability, which ranges from 1·8 GPa to 2·5 GPa on the wet solidus. Furthermore, despite simple rules that can be applied to evaluate the relevance of a specific assemblage in simple chemical systems (e.g Mg/Si ratio for the 10 Å phase, Fumagalli *et al.*, 2001; Stalder & Ulmer, 2001; Fe–Mg partitioning for MgMgAl-pumpellyite–sursassite, Artioli *et al.*, 1999; Bromiley & Pawley, 2003), more complex relationships hold in natural systems containing a large number of independent chemical components. Again, the mutual stability of chlorite, DHMS and anhydrous solid solutions in complex bulk compositions is substantially unknown; it is worth noting that the absence of low-temperature data for such compositions also hampers verification of geothermobarometers for peridotites in cold tectonic environments.

This experimental work aims to unravel subsolidus phase relationships in variably enriched ultramafic compositions modelled in the system $Na_2O–CaO–FeO–MASH$ (NCFMASH). Particular emphasis will be given to hydrous phases such as chlorites, amphiboles and DHMS and their mutual relations, so as to evaluate and depict the contribution of the ultramafic portion of the slab to the water budget in subduction zones.

EXPERIMENTAL PROCEDURES

Starting materials

Although the layered structure of the oceanic lithosphere has been widely recognized, sampling of modern ocean floors and ophiolites suggests rather complex structural and chemical heterogeneities. Although harzburgites and variably enriched lherzolites (Baker & Beckett, 1999) represent the most notable upper-mantle lithologies, the occurrence of layers or veins of pyroxenites is testified from abyssal dredges, alpine massifs, mantle xenoliths and ophiolites (Hirschmann & Stolper, 1996; Salters & Dick, 2002). A wide compositional range of ultramafic lithologies is, therefore, expected to contribute to the total water budget in subduction-zone environments.

Hydrous peridotites have been modelled in the chemical system $Na_2O–CaO–FeO–MgO–Al_2O_3–SiO_2–H_2O$ (NCFMASH). Three model compositions have been investigated (Table 1): PX, approximating an Hawaiian peridotite nodule that represents an olivine-poor garnet lherzolite [composition D-66SAL-1 of Mysen & Boettcher (1975)]; LZ, the Tinaquillo lherzolite (Green, 1963); HZ, a harzburgite dredged from the ocean floor (Hebert *et al.*, 1983). PX shows a significant content of basaltic component and as a result it is enriched in Al_2O_3, CaO and Na_2O, and also has a relatively low X_{Mg} value, where $X_{Mg} = Mg/(Mg + Fe^{tot})$. Such a composition represents a useful end-member for the definition of phase diagrams, allowing a maximum occurrence of aluminous phases. A similar approach was followed by Niida & Green (1999), who investigated the amphibole mineral chemistry in ultramafic rocks. In particular, the composition referred to by those workers as HPY-40% Ol is comparable with the olivine-poor lherzolite composition of this study.

To promote the synthesis at subsolidus conditions, gels have been prepared following the method of Hamilton & Henderson (1968) using tetraethylorthosilicate (TEOS) as silica source, pure Na–, Ca–, Mg– and Al–nitric solutions, and ferric benzoate. Gels were fired in a gas mixing furnace at fO_2 conditions approaching the FMQ (fayalite–magnetite–quartz) buffer at 1 atm, then seeded with mineral phases expected to be stable in the pressure range investigated here. Individual seed compositions largely differ from the stable compositions expected at the P–T conditions investigated to favour unquestionable identification of relicts, but the composition of the seed mixture closely reproduces the bulk composition chosen to avoid fractionation. Seed mixtures are composed of 34·58 wt % natural clinochlore (Val Malenco, Italy),

Table 1: Compositions of starting materials

	PX	LZ	HZ
SiO_2	45·41	45·75	45·63
Al_2O_3	8·26	3·33	1·46
FeO	9·81	7·03	9·62
MgO	27·38	40·59	42·42
CaO	8·32	3·11	0·57
Na_2O	0·82	0·19	0·30
Total	100·00	100·00	100·00
X_{Mg}	0·83	0·91	0·89

PX, model Hawaiian peridotite nodule (Mysen & Boettcher, 1975) with 10% added seed mixture; LZ, model Tinaquillo lherzolite (Green, 1963) with 1·26% added seed mixture; HZ, model harzburgite from the ocean floor (Hebert *et al.*, 1983) with 1% added seed mixture.

7·44 wt % natural pyrope (Dora Maira, Italy), 36·94 wt % synthetic diopside and 21·04 wt % synthetic forsterite (Fo_{70}). Mixtures were added in amounts of 10 wt % in PX, 1·26 wt % in LZ and 1 wt % in HZ.

Experimental conditions and apparatus

High-pressure experiments were performed at pressures ranging from 2·0 GPa to 6·5 GPa and temperatures from 680°C to 800°C at the Dipartimento di Scienze della Terra in Milano, Italy. Pressures up to 3·0 GPa were investigated in piston cylinders, both single stage (up to 2·4 GPa) and end loaded (up to 3·0 GPa) using full salt and MgO–salt assemblies, respectively. Temperature was measured by K-type and S-type thermocouples and was considered accurate to ±5°C. A Walker-type multianvil apparatus was used for higher pressures using tungsten carbide cubes of 32 mm edge length and 17 mm truncation edge length (TEL), and pressure cells made of prefabricated MgO octahedra (containing 5 wt % of Cr_2O_3) with a 25 mm edge length (25 M). Multianvil pressure calibration was performed both at room temperature, using the phase transitions Bi I–II, Bi III–V (respectively at 2·55 and 7·7 GPa), and, at 1000°C, the coesite–stishovite and $CaGeO_3$ garnet–perovskite transitions occurring respectively at 8·7 GPa (Zhang *et al.*, 1996) and 6·1 GPa (Susaki *et al.*, 1985). Pressure uncertainties, which largely depend on the accuracy of the calibrant reaction, were assumed to be ±3%. Further details have been given by Fumagalli & Poli (1999). Temperature was measured by S-type thermocouples and was considered accurate to ±20°C without taking into account any effect of pressure on the e.m.f. of the thermocouple.

Gold capsules (outer diameter 3·0 mm, length 3·5 mm) were welded after being loaded with 10–15 mg of seeded gel and 10 wt % of distilled water. All runs were at fluid-saturated conditions.

Table 2: Experimental run conditions

Run number	Pressure (GPa)	Temperature (°C)	Time (h)	Starting material	Run products
Px8 (SS-PC)	2·0	800	1440	PX	ol, opx, gar, amp
Px9 (SS-PC)	2·2	700	360	PX	ol, cpx, amp, chl
Px11 (SS-PC)	2·4	700	500	PX	ol, cpx, amp
Px10 (EL-PC)	2·6	700	500	PX	ol, cpx, chl
Px7 (EL-PC)	3·0	800	256·2	PX	ol, opx, cpx, gar
Px6 (MA)	4·2	680	271·1	PX	ol, gar, cpx, chl
Px2 (MA)	4·6	750	111	PX	ol, opx, cpx, gar
Px5 (MA)	4·8	680	151·3	PX	ol, gar, cpx, 10 Å
Px3 (MA)	5·2	680	170·4	PX	ol, gar, cpx, 10 Å
Lz1 (SS-PC)	2·2	700	720	LZ	ol, amp, chl
Lz4 (SS-PC)	2·4	700	500	LZ	ol, amp, chl
Lz3 (EL-PC)	2·6	700	500	LZ	ol, opx, cpx, chl
Lz2 (EL-PC)	3·0	750	197	LZ	ol, opx, cpx, chl
Lz5 (MA)	6·0	680	175·7	LZ	ol, cpx, gar, 10 Å, opx
Lz7 (MA)	6·0	750	351	LZ	ol, opx, cpx, gar
Lz10 (MA)	6·5	650	168	LZ	ol, cpx, gar, 10 Å
Lz9 (MA)	6·5	700	479	LZ	ol, opx, cpx, gar
Hz3 (SS-PC)	2·2	700	720	HZ	ol, amp, opx, chl
Hz2 (MA)	4·2	680	250	HZ	ol, opx, cpx, chl
Hz1 (MA)	5·2	680	240	HZ	ol, opx, cpx, 10 Å

PX, olivine-poor lherzolite; LZ, Tinaquillo lherzolite; HZ, harzburgite; ol, olivine; opx, orthopyroxene; cpx, clinopyroxene; chl, chlorite; amp, amphibole; gar, garnet; 10 Å, 10 Å phase; SS-PC, single-stage piston cylinder; EL-PC, end-loaded piston cylinder; MA, multi-anvil.

Oxygen fugacity was constrained by adding graphite to the charges on the basis of the following assumptions: (1) at high-pressure, low-temperature conditions the graphite-saturated surface in the system C–O–H (i.e. the 'graphite boundary') approaches the H_2O component ($XH_2O = 0{\cdot}99987$ at 5 GPa, 700°C, H:O = 2); (2) at temperature conditions below 700°C diffusion of hydrogen in gold is negligible (Chou, 1986); (3) given the relatively high amount of H_2O added to the gels and the low Fe content of the starting material, redox reactions are assumed to have negligible effect on the fluid, therefore the H:O ratio can be safely assumed to be fixed at 2:1. As a result, a mixture of C + H_2O 'buffers' the volatile species in the fluid and H_2O activity is calculated to approach unity (>0·999). Estimates of oxygen fugacity were calculated by maximizing the XH_2O in the fluid (Connolly & Cesare, 1993); experimental oxidation states at 700°C range from *c.* FMQ – 1·7 at 3·0 GPa to FMQ + 0·2 at 6·0 GPa.

As experimental temperatures were low, runs lasted up to 2 months (Table 2).

Run products were first characterized by X-ray powder diffraction on a Philips APD 1000 diffractometer and inspected on back-scattered electron (BSE) and secondary electron images. An ARLK microprobe with six wavelength-dispersive spectrometers was used for microanalysis. Beam conditions were set to 15 kV and 20 nA. Silicates were used as standards and data processed with a ZAF correction procedure.

Approach to equilibrium

It is beyond the goal of this work to perform reversal experiments. The low temperatures investigated do not favour kinetics and the results of bracketing reactions are extremely difficult to assess once reactivity of the starting material is lost (e.g. using a crystal mixture as in traditional bracketing techniques). Furthermore, because most phase boundaries are controlled by continuous reactions involving multicomponent solid solutions, recognition of bracketing is nearly impossible in such complex systems, when phase abundance and mineral chemistry vary smoothly.

Although seeds favour crystallization, their behaviour has to be taken into account to assess the attainment to equilibrium. Textural observations suggest that growth rather than nucleation usually involves seeds. Although some seed relics, especially garnet, are not completely resorbed, the compositional homogeneity of the growth rims and the sharp boundary between pre-existing seeds of known composition and newly crystallized phases suggest that the latter phases approach equilibrium.

Systematic and consistent variations in mineral chemistry in different environmental conditions, as well as coherent element partitioning, strongly support approach to equilibrium (see below). Mass-balance and chemographic analysis provide constraints against macroscopic fractionation processes in the charge (possibly occurring in fluid-saturated experiments; Schmidt & Ulmer, 2004).

Imaging offers an additional perspective on textural readjustment and on interfacial equilibrium (see below).

RESULTS

Phase assemblages

Experimental run details are shown in Table 2. The most representative data are those obtained in compositions PX and LZ. The fine-grained features of products in the harzburgite composition together with the extremely low content of Al_2O_3 and CaO made the microprobe chemical analysis particularly difficult. Data reported for this composition are, therefore, restricted to a preliminary characterization of phase assemblages by X-ray powder diffractometry.

Phase relationships for the three compositions investigated are summarized in Fig. 1. Phase boundaries in the low-temperature region, dominated by the occurrence of antigorite, are from Ulmer & Trommsdorff (1999). At temperatures above antigorite stability, phase boundaries for hydrous phases are drawn schematically as their dependence on the bulk compositions is unresolved. The spinel–garnet transition represented in Fig. 1 (dashed grey line) results from phase assemblages observed in one experiment performed on the PX composition. Niida & Green (1999), on the basis of experiments performed on natural compositions (MORB Pyrolite), located the spinel–garnet transition at 2·0 GPa, 1050°C and its extrapolation to lower temperatures is represented in Fig. 1 by the dotted curve a. The absence of Cr and the relatively low Mg value of the olivine-poor lherzolite composition used in this study ($X_{Mg} = 0{\cdot}83$) compared with the Niida & Green bulk composition ($X_{Mg} = 0{\cdot}88$) account for the shift of the garnet-in reaction towards lower pressure: the lack of Cr reduces the stability of spinel and the higher Fe^{2+} favours garnet stability at lower pressure (O'Neill, 1981; Gasparik, 1987).

Amphibole and chlorite

The location and dP/dT slope of amphibole breakdown are constrained by experiments presented here, by near-solidus experiments of Green (1973), Milhollen *et al.* (1974), Mysen & Boettcher (1975), Mengel & Green (1989), Wallace & Green (1991) and Niida & Green (1999), and by the low-temperature topology of the amphibole breakdown reactions summarized by Schmidt & Poli (1998). Although bulk composition is expected to influence the location of amphibole breakdown (Wallace & Green, 1991; Niida & Green, 1999) we did not observe any significant shift of amphibole breakdown at 700°C in PX and LZ. Amphibole pressure stability at higher temperatures is tentatively drawn in Fig. 1 connecting experimental constraints given here with the location of amphibole-out on the wet solidus given by Wallace & Green (1991) and Niida & Green (1999). Furthermore, whether a two-pyroxene- or one-pyroxene-bearing assemblage is stable is also dependent on whole-rock bulk composition.

Chlorite breakdown with temperature in Fig. 1 mimics the model reaction

$$\text{clinochlore} + \text{enstatite} = \text{forsterite} + \text{pyrope} + H_2O \quad (1)$$

in the system MASH (Pawley, 2003),and chlorite breakdown reactions at lower pressures [see Ulmer & Trommsdorff (1999) for a review], although it will be shown below that clinopyroxene is a major phase involved in chlorite disappearance.

In the olivine-poor lherzolite composition amphibole and chlorite coexist together with clinopyroxene at

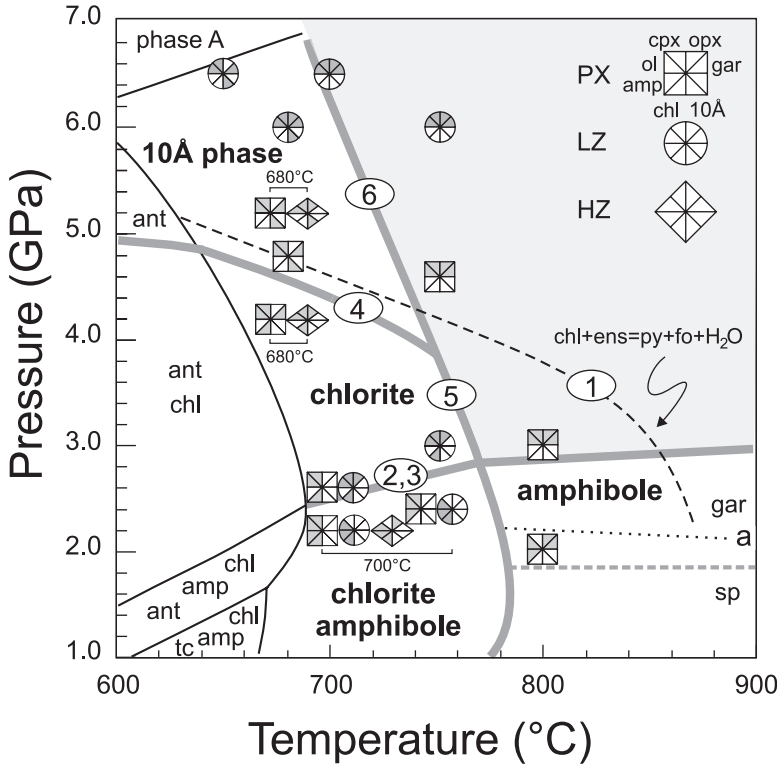

Fig. 1. Phase assemblages in olivine-poor lherzolite (squares), Tinaquillo lherzolite (circles), and harzburgite (diamonds) compositions at fluid-saturated conditions as a function of pressure and temperature. Phase relationships involving antigorite (ant) are from Ulmer & Trommsdorff (1999); topology of amphibole breakdown reactions is from Schmidt & Poli (1998). Numbers refer to reactions discussed in text. chl, chlorite; amp, amphibole; ol, olivine; cpx, clinopyroxene; opx, orthopyroxene; gar, garnet; 10 Å, 10 Å phase; sp, spinel; tc, talc. The dashed grey line (this study) and curve a (Niida & Green, 1999; MORB pyrolite) show the shift of the transition from spinel peridotites to garnet peridotites as a function of the bulk composition chosen. The grey field represents absence of stable hydrous phases.

2·2 GPa, 700°C. Low-angle X-ray powder Bragg diffraction allows a straightforward identification of coexisting chlorite and amphibole. Textural observations show euhedral amphiboles up to 20 μm in a finer matrix composed of intergrowths of clinopyroxene and chlorite. At 2·4 GPa, 700°C no chlorite was identified and euhedral amphibole up to 20 μm in size coexists with olivine in a finer clinopyroxene matrix. At 2·6 GPa, 700°C an unexpected three-phase assemblage was found that consisted of chlorite, olivine and clinopyroxene.

In the Tinaquillo lherzolite amphibole and chlorite coexist with olivine at 2·2 and 2·4 GPa, 700°C. BSE images show round-shaped olivine in a matrix of chlorite aggregates up to 5–10 μm in size and elongated euhedral crystals of amphibole up to 5 μm in size. Pseudomorphic textures have been recognized, suggesting presumably garnet seeds replaced by chlorite at the core and amphibole at the rim.

In the olivine-poor lherzolite chlorite disappears at 2·0 GPa, 800°C and amphibole is stable together with garnet, olivine and orthopyroxene. BSE images show megacrystals of orthopyroxene up to 100 μm often including all the other phases, euhedral amphibole, garnet and olivine. The occurrence of numerous triple points involving both garnet and olivine (Fig. 2a) suggests a well-equilibrated texture. At 4·2 GPa and 680°C, aggregates of chlorite of up to 10 μm appear (Fig. 2b) together with euhedral olivine (up to 5–10 μm), garnet (up to 10–15 μm) and polycrystalline aggregates of clinopyroxene (up to 15 μm).

10 Å phase

From 4·8 GPa, 680°C a 10 Å phase structure was found to replace chlorite in all compositions investigated (Fig. 2c). Although the 10 Å phase represents an experimental run product first synthesized in the MSH system (Sclar *et al.*, 1965), its natural occurrence has been proposed in chlorite-rich peridotite xenoliths from the diatreme at Moses Rocks (Colorado Plateau, Utah) by Smith (1995). The 10 Å phase structure (Sclar *et al.*, 1965; Yamamoto & Akimoto, 1977; Bauer & Sclar, 1981; Wunder & Schreyer, 1992; Pawley & Wood, 1995; Fumagalli *et al.*, 2001) in run products was recognized by X-ray powder diffractometry mainly on the basis of the sharp basal peak at $d = 10{\cdot}34$ Å. The X-ray diffraction

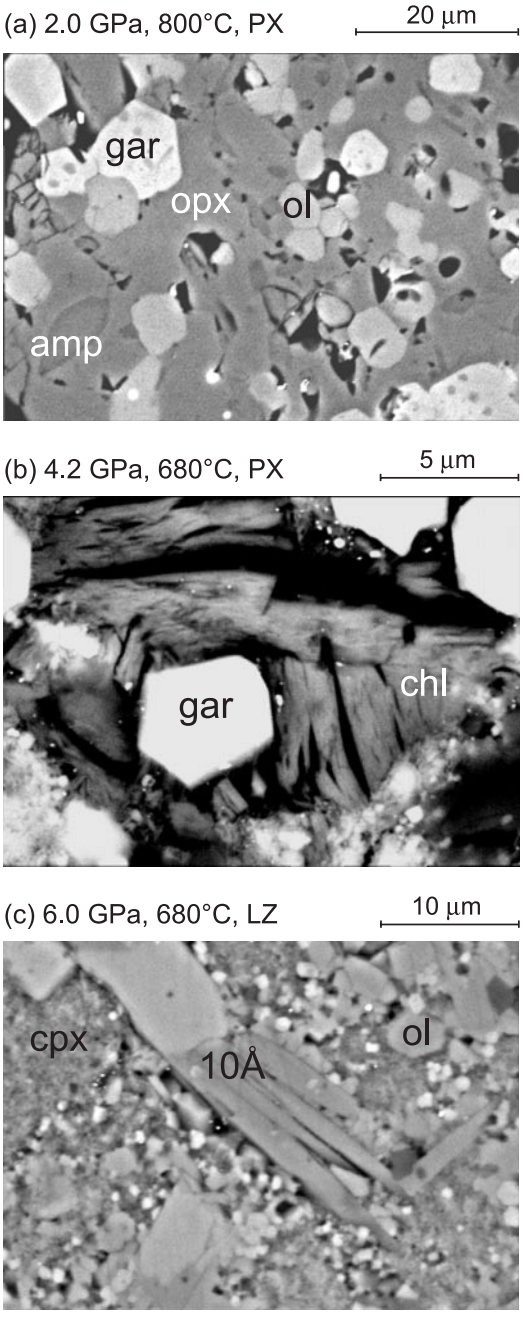

Fig. 2. Back-scattered electron images of experimental charges. (a) Poikilitic crystal of orthopyroxene including texturally equilibrated crystals of olivine, amphibole and garnet; run time 256 h. (b) Subidiomorphic garnet and chlorite; 271 h. (c) Sheets of 10 Å phase in a fine-grained matrix of olivine and clinopyroxene; 175 h.

pattern of run products (10 Å phase, garnet, olivine and clinopyroxene) obtained at 4·8 GPa, 680°C in the olivine-poor lherzolite is shown in Fig. 3. Although it is beyond the goal of this work to discuss details of the crystallographic properties of the 10 Å phase and coexisting phases, the diffraction pattern was refined by the Rietveld method to estimate lattice parameters and phase abundances (see also the section on mass-balance calculations). Mineral compositions obtained by microprobe analysis have been used in calculations and a phlogopite structure has been considered for the 10 Å phase structure, in which the 12-coordinated interlayer site usually occupied by potassium was considered to be occupied by water molecules [see Fumagalli *et al.* (2001) for details]. At lower values of 2θ, the diffraction pattern shows in addition a peak at $d = 14{\cdot}80$ Å ($2\theta = 5{\cdot}96°$), a value approaching the 001 diffraction of clinochlore, at $d = 14{\cdot}20$ Å ($2\theta = 6{\cdot}25°$), but significantly higher than this. Because clinochlore was not detected by electron microprobe, such diffraction is attributed to crystallographic features of the 10 Å phase, as discussed below.

The 10 Å phase structure forms aggregates (10–15 μm) of platy crystals coexisting with euhedral garnet (up to 10 μm) in a finer matrix of olivine and clinopyroxene intergrowths.

The anhydrous assemblage garnet, olivine, clinopyroxene and orthopyroxene was found at 3·0 GPa, 800°C and 4·6 GPa, 750°C in the olivine-poor lherzolite and at 6·0 GPa, 750°C and 6·5 GPa, 700°C in the Tinaquillo lherzolite.

Mineral chemistry

Olivine

X_{Mg} [$X_{Mg} = Mg/(Mg + Fe^{tot})$] ranges from 0·81 to 0·88 in the olivine-poor lherzolite, and from 0·89 to 0·92 in the Tinaquillo lherzolite, reflecting the bulk composition (Table 3). The X_{Mg} of olivine slightly increases with pressure both in the olivine-poor lherzolite and in the Tinaquillo lherzolite as a result of the appearance of garnet, which, having lower X_{Mg}, favours a higher Mg content in coexisting phases at fixed bulk composition.

Orthopyroxene

There is a similar dependence of the X_{Mg} value on bulk composition (X_{Mg} is 0·84–0·88 in the olivine-poor lherzolite and 0·90–0·93 in the Tinaquillo lherzolite; Table 4). Aluminium content in orthopyroxene ranges from 0·016 to 0·210 a.p.f.u. and is anticorrelated with pressure.

Clinopyroxene

X_{Mg} ranges from 0·81 to 0·90 in the olivine-poor lherzolite and from 0·92 to 0·94 in the Tinaquillo lherzolite (Table 5). Because of the high pressure investigated, the Ca-Eskola component has been taken into account following Katayama *et al.* (2000). The results suggest, however, that the Ca-Eskola component is negligible, allowing us to assume stoichiometric clinopyroxenes. Significant variations in the aluminium and sodium content of clinopyroxenes have been observed in the olivine-poor lherzolite composition. In particular, the

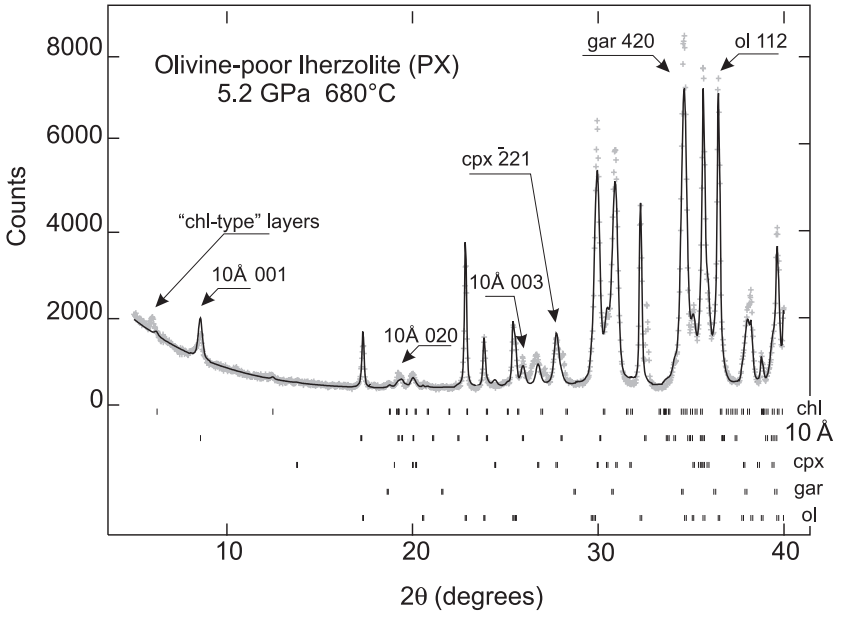

Fig. 3. X-ray diffraction profile of run products in the olivine-poor lherzolite composition at 5·2 GPa, 680°C. +, observed profile; the continuous line is the calculated profile obtained by Rietveld refinement. Diffraction patterns of the phases present are, from the bottom to the top: olivine (ol), garnet (gar); clinopyroxene (cpx); 10 Å phase structure (10 Å); clinochlore (chl). The most representative diffractions are also indicated on the profile itself.

aluminium and sodium contents decrease with pressure up to 3·0 GPa, but increase at higher pressure, suggesting that the increasing jadeitic component in clinopyroxene is buffered at pressures lower than 3·0 GPa by a Na-bearing phase, amphibole, whereas at higher pressures this is dependent on the bulk composition of the starting material.

Garnet

Attempts to optimize the charge balance result in particularly high values of ferric iron, with Fe^{3+}/Fe^{tot} ratios reaching 0·3 (Px5, 4·8, 680°C). Potentially overestimated amounts of Fe^{3+} may indicate a charge deficiency in the X site, occupied by Mg, Fe^{2+} and Ca. Strong differences between the Fe^{3+}/Fe^{tot} ratio calculated from microprobe analysis and obtained by Mössbauer spectroscopy have been widely demonstrated (e.g. Luth *et al.*, 1990). On the other hand, experimental results have shown that the Fe^{3+} substitution in garnet solid solution, i.e. the amount of skiagite component ($Fe_3Fe_2Si_2O_{12}$) and andradite ($Ca_3Fe_2Si_3O_{12}$), strongly increases with pressure (Woodland & O'Neill, 1993, 1995). Although interlaboratory duplicates (Milan, Clermont-Ferrand, Ann Arbor) of analytical results performed on the same experimental charges have confirmed the requirement of a significant amount of Fe^{3+}, crystal chemical complexities remain unresolved without further crystallographic investigations. As a consequence, the normalization procedure adopted accounts for all iron as Fe^{2+}.

Garnets are compositionally pyrope rich (Table 6) and show relatively high Ca contents.

Amphibole

Analyses are normalized on the basis of 23 oxygens and, because of the artefacts introduced in normalization schemes for amphibole, we assume all iron as Fe^{2+} (Table 7). This also allows us directly to compare amphiboles synthesized by Mysen & Boettcher (1975) and Niida & Green (1999), who used the same normalization procedure. It is worth noting that the analyses given by those workers are the only Fe-bearing amphibole compositions at subsolidus conditions in the pressure range of interest here, and that data below 900°C are completely unavailable to date. Following Leake *et al.* (1997), experimental amphiboles in runs Px8 and Px11 are pargasites because of their higher Al and Na content; Px9 amphiboles are high in SiO_2, trending, therefore, towards edenite, and low in Al_2O_3, suggesting a significant tremolite–actinolite substitution. Amphiboles in the Tinaquillo lherzolite are tremolite–actinolite with a small Na-amphibole component. However, given the fine-grained texture of runs Lz1 and Lz4 the crystal chemistry of amphiboles may be biased by analytical difficulties. Mg values range from 0·83–0·86 for the olivine-poor lherzolite composition to 0·92 for the Tinaquillo lherzolite, in agreement with the Mg values of the starting materials. As expected, the trend defined by amphibole composition as a whole is consistent with the dominance of a pargasite substitution

Table 3: Wavelength-dispersive (WDS) chemical compositions of olivines

Run:	Px8	Px11	Px7	Px6	Px2	Px5	Px3
P (GPa):	2·0	2·4	3·0	4·2	4·6	4·8	5·2
T (°C):	800	700	800	680	750	680	680
SiO_2	39·85 (0·75)	39·93 (0·67)	41·39 (0·68)	40·99 (0·97)	41·44 (0·41)	40·69 (0·87)	40·10 (0·02)
Al_2O_3	0·08 (0·10)	0·15 (0·15)	0·08 (0·03)	0·25 (0·30)	0·13 (0·09)	0·07 (0·02)	0·16 (0·11)
FeO	17·11 (0·57)	18·20 (0·92)	11·33 (1·20)	13·10 (0·24)	14·10 (1·05)	13·43 (0·39)	13·49 (1·72)
MgO	44·74 (1·28)	42·45 (0·87)	48·87 (3·35)	46·29 (1·40)	45·08 (1·51)	47·56 (1·65)	44·31 (0·36)
CaO	0·21 (0·10)	0·26 (0·14)	0·22 (0·08)	0·24 (0·13)	0·23 (0·10)	0·17 (0·01)	0·24 (0·02)
Na_2O	0·00 (0·01)	0·01 (0·02)	0·09 (0·02)	0·14 (0·09)	0·02 (0·03)	0·04 (0·04)	0·00 (0·00)
Total	101·99	101·00	101·99	101·00	101·00	101·95	98·30
Si	0·986 (0·028)	1·010 (0·009)	1·000 (0·034)	1·010 (0·025)	1·030 (0·022)	0·993 (0·032)	1·020 (0·016)
Al	0·002 (0·003)	0·005 (0·005)	0·002 (0·001)	0·007 (0·008)	0·004 (0·003)	0·002 (0·000)	0·005 (0·003)
Fe^{2+}	0·354 (0·010)	0·385 (0·018)	0·229 (0·025)	0·270 (0·005)	0·293 (0·019)	0·274 (0·011)	0·287 (0·032)
Mg	1·650 (0·029)	1·600 (0·017)	1·760 (0·046)	1·700 (0·028)	1·670 (0·026)	1·730 (0·040)	1·680 (0·016)
Ca	0·006 (0·003)	0·007 (0·004)	0·006 (0·002)	0·006 (0·003)	0·006 (0·003)	0·004 (0·000)	0·006 (0·000)
Na	0·000 (0·000)	0·000 (0·001)	0·004 (0·001)	0·007 (0·005)	0·001 (0·001)	0·002 (0·002)	0·000 (0·000)
X_{Mg}	0·82 (0·00)	0·81 (0·01)	0·88 (0·01)	0·86 (0·00)	0·85 (0·01)	0·86 (0·01)	0·85 (0·01)

Run:	Lz1	Lz4	Lz3	Lz2	Lz5	Lz7	Lz10	Lz9
P (GPa):	2·2	2·4	2·6	3·0	6·0	6·0	6·5	6·5
T (°C)	700	700	700	750	680	750	650	700
SiO_2	41·60 (1·81)	41·02 (0·54)	41·25 (0·47)	41·54 (1·14)	40·74 (0·90)	39·73 (0·96)	41·41 (1·28)	41·88 (0·97)
Al_2O_3	0·12 (0·14)	0·17 (0·22)	0·08 (0·06)	0·10 (0·09)	0·06 (0·02)	0·03 (0·07)	0·11 (0·18)	0·33 (0·46)
FeO	10·20 (0·37)	9·49 (0·31)	11·01 (0·20)	10·28 (0·34)	8·29 (0·24)	18·41 (6·33)	8·53 (0·35)	7·71 (0·42)
MgO	49·97 (1·72)	51·00 (1·12)	49·51 (0·68)	49·89 (0·53)	51·81 (0·58)	43·57 (4·67)	49·79 (1·98)	49·87 (2·02)
CaO	0·10 (0·10)	0·09 (0·10)	0·04 (0·02)	0·07 (0·03)	0·09 (0·04)	0·16 (0·09)	0·12 (0·11)	0·11 (0·11)
Na_2O	0·01 (0·01)	0·00 (0·01)	0·01 (0·01)	0·00 (0·00)	0·01 (0·01)	0·00 (0·00)	0·05 (0·06)	0·00 (0·00)
Total	101·99	101·78	101·90	101·89	101·00	101·90	100·00	99·90
Si	1·000 (0·036)	0·982 (0·013)	0·995 (0·008)	1·000 (0·016)	0·976 (0·007)	0·991 (0·007)	1·010 (0·023)	1·020 (0·022)
Al	0·003 (0·004)	0·005 (0·006)	0·002 (0·002)	0·003 (0·002)	0·002 (0·001)	0·001 (0·002)	0·003 (0·005)	0·010 (0·013)
Fe^{2+}	0·205 (0·011)	0·190 (0·006)	0·222 (0·004)	0·207 (0·007)	0·166 (0·003)	0·384 (0·134)	0·174 (0·009)	0·157 (0·008)
Mg	1·790 (0·037)	1·820 (0·017)	1·780 (0·009)	1·790 (0·015)	1·850 (0·009)	1·620 (0·138)	1·810 (0·024)	1·810 (0·030)
Ca	0·002 (0·003)	0·002 (0·003)	0·001 (0·000)	0·002 (0·001)	0·002 (0·001)	0·004 (0·002)	0·003 (0·003)	0·003 (0·003)
Na	0·000 (0·001)	0·000 (0·000)	0·000 (0·000)	0·000 (0·000)	0·000 (0·000)	0·000 (0·000)	0·002 (0·003)	0·000 (0·000)
X_{Mg}	0·90 (0·00)	0·91 (0·00)	0·89 (0·00)	0·90 (0·00)	0·92 (0·00)	0·81 (0·07)	0·91 (0·00)	0·92 (0·01)

$X_{Mg} = Mg/(Mg + Fe^{tot})$. Values in parentheses are the 1σ standard deviations.

(Fig. 4a and b). In Fig. 4c we report the content of total Na in amphibole coexisting with Na-bearing clinopyroxene as a phase buffering Na-exchange vectors. Comparison with data previously obtained by Mysen & Boettcher (1975) and Niida & Green (1999) reveals a strong temperature dependence of Na content in amphibole and a very modest, if any, pressure dependence. This possibly modifies at low temperature the schematic arrangement of Na isopleths proposed by Niida & Green (1999).

Chlorite

It is compositionally close to clinochlore, with X_{Mg} value ranging from 0·85 to 0·92 in the olivine-poor lherzolite and from 0·94 to 0·95 in the Tinaquillo lherzolite in agreement with the different starting materials (Table 8). The X_{Mg} value decreases with pressure up to 3·0 GPa. Although data are limited to the run at 4·2 GPa and 680°C, it should be preliminarily noted that an opposite trend has been observed at higher pressure, when chlorite

Table 4: WDS chemical compositions of orthopyroxenes

Run:	Px8	Px7	Px2	Lz3	Lz2	Lz5	Lz7	Lz9
P (GPa):	2·0	3·0	4·6	2·6	3·0	6·0	6·0	6·5
T (°C):	800	800	750	700	750	680	750	700
SiO_2	54·03 (0·55)	55·83 (0·65)	57·06 (1·50)	55·98 (0·50)	58·48 (1·21)	56·66 (1·19)	58·49 (2·42)	57·22 (0·23)
Al_2O_3	5·15 (0·30)	1·16 (0·26)	0·63 (0·37)	0·38 (0·11)	0·49 (0·07)	0·83 (0·68)	0·39 (0·52)	1·06 (1·50)
Fe_2O_3	0·01 (0·03)	0·31 (0·11)	0·09 (0·12)	0·25 (0·10)	0·01 (0·02)	0·15 (0·16)	0·00 (0·00)	0·00 (0·00)
FeO	10·47 (0·37)	7·72 (0·72)	8·61 (0·45)	6·49 (0·42)	6·61 (0·21)	5·14 (0·26)	4·90 (0·44)	4·94 (0·47)
MgO	31·60 (0·35)	32·16 (0·59)	34·95 (0·74)	32·81 (1·27)	36·07 (0·30)	36·65 (0·86)	35·91 (2·15)	35·29 (0·35)
CaO	0·57 (0·08)	0·84 (0·24)	0·61 (0·56)	1·99 (0·89)	0·28 (0·17)	0·50 (0·46)	0·18 (0·22)	0·38 (0·32)
Na_2O	0·01 (0·01)	0·12 (0·04)	0·04 (0·05)	0·10 (0·04)	0·00 (0·01)	0·06 (0·06)	0·00 (0·00)	0·00 (0·00)
Total	101·84	98·15	101·99	98·00	101·93	99·99	99·88	98·89
Si	1·870 (0·009)	1·980 (0·014)	1·950 (0·049)	1·980 (0·015)	1·980 (0·012)	1·950 (0·025)	2·000 (0·032)	1·980 (0·035)
Al	0·210 (0·012)	0·049 (0·011)	0·025 (0·015)	0·016 (0·005)	0·020 (0·003)	0·034 (0·028)	0·016 (0·020)	0·043 (0·061)
Fe^{3+}	0·000 (0·001)	0·008 (0·003)	0·002 (0·003)	0·007 (0·003)	0·000 (0·001)	0·004 (0·004)	0·000 (0·000)	0·000 (0·000)
Fe^{2+}	0·303 (0·010)	0·229 (0·021)	0·246 (0·013)	0·192 (0·011)	0·187 (0·005)	0·148 (0·008)	0·140 (0·010)	0·143 (0·012)
Mg	1·630 (0·020)	1·700 (0·036)	1·780 (0·040)	1·730 (0·049)	1·820 (0·021)	1·880 (0·042)	1·830 (0·060)	1·820 (0·044)
Ca	0·021 (0·003)	0·032 (0·009)	0·022 (0·020)	0·075 (0·035)	0·010 (0·006)	0·018 (0·017)	0·007 (0·008)	0·014 (0·012)
Na	0·000 (0·001)	0·008 (0·003)	0·002 (0·003)	0·007 (0·003)	0·000 (0·001)	0·004 (0·004)	0·000 (0·000)	0·000 (0·000)
X_{Mg}	0·84 (0·01)	0·88 (0·01)	0·88 (0·00)	0·90 (0·00)	0·91 (0·00)	0·93 (0·00)	0·93 (0·01)	0·93 (0·01)

$X_{Mg} = Mg/(Mg + Fe^{tot})$.

coexists with garnet. The aluminium content, which slightly decreases with pressure, ranges from 3·170 to 3·730 a.p.f.u. in the olivine-poor lherzolite and from 2·570 to 4·000 a.p.f.u. in the Tinaquillo lherzolite.

10 Å phase

Microanalyses on aggregates were normalized on the basis of seven cations and 11 oxygens following the chemical formula of the 10 Å phase in the MSH system $Mg_3Si_4O_{10}(OH)_2{\cdot}nH_2O$, although free water molecules were not taken into account (Table 9). The X_{Mg} values reflect the Mg values of the starting materials (0·91–0·92 for the olivine-poor lherzolite and 0·94–0·95 for the Tinaquillo lherzolite). For both compositions a significant amount of aluminium has been detected in the 10 Å phase, which ranges from 9·01 to 10·53 wt %, corresponding to about 0·7–0·8 a.p.f.u. incorporated into the 10 Å phase structure.

Although a Tschermak component is a reasonable candidate to explain the aluminium content of this sheet silicate, it is actually inconsistent with the mineral chemistry obtained from microprobe analysis. A Tschermak-related Al content of 0·8 a.p.f.u. would imply the stoichiometry $(Mg+Fe^{2+})_{2.6}Al^{VI}_{0.4}Si_{3.6}Al^{VI}_{0.4}O_{10}(OH)_2$, which is generally less than the $(Mg + Fe^{2+})$ and in excess of the Si values found, which are in the range of 2·943–3·266 and 3·030–3·120, respectively.

An alternative explanation for the relatively high aluminium content in the Al-10 Å phase is shown in Fig. 5. Its composition both in the olivine-poor lherzolite and in the Tinaquillo lherzolite is surprisingly coincident with a mixed layered structure formed of clinochlore and talc in the proportion of 1:1, found in nature and called kulkeite by Schreyer *et al.* (1982). It should be recalled here that the anhydrous chemical composition of the 10 Å phase is coincident with that of talc, and that the 10 Å phase has been regarded as a hydrated talc stable at high pressure (Pawley & Wood, 1995; Chinnery *et al.*, 1999). Coincidence with kulkeite stoichiometry might, therefore, suggest the occurrence of a mixed layered chlorite–10 Å phase structure, and a discussion of the consequences of this will be given below.

DISCUSSION

Fe–Mg partitioning

It is beyond the goal of this study to consider in detail the widely used geothermometers based on iron and magnesium partitioning (e.g. garnet–orthopyroxene, garnet–clinopyroxene, garnet–olivine). Nevertheless, a comparison of calculated element partitioning and the experimental data provide an opportunity to verify the internal consistency of the analytical data reported here and to estimate the predictive ability of current

Table 5: WDS chemical compositions of clinopyroxenes

Run:	Px9	Px11	Px10	Px7	Px6	Px2	Px5
P (GPa):	2·2	2·4	2·6	3·0	4·2	4·6	4·8
T (°C):	700	700	700	800	680	750	680
SiO_2	50·67 (1·63)	51·65 (1·65)	52·18 (2·96)	54·53 (1·18)	52·30 (1·29)	53·22 (1·41)	51·58 (2·77)
Al_2O_3	4·25 (1·81)	5·98 (1·09)	3·13 (1·67)	1·35 (0·58)	2·10 (0·76)	4·56 (1·42)	3·41 (0·07)
FeO	7·18 (0·29)	3·66 (0·32)	7·02 (1·20)	4·05 (1·08)	4·50 (1·38)	6·13 (0·99)	5·01 (0·34)
MgO	17·27 (1·20)	17·99 (0·86)	19·06 (2·01)	20·32 (0·83)	17·54 (0·91)	19·07 (1·06)	18·66 (0·73)
CaO	18·12 (2·45)	18·16 (0·89)	17·85 (3·55)	18·46 (2·30)	20·66 (2·21)	17·11 (1·59)	17·54 (2·01)
Na_2O	0·67 (0·12)	0·76 (0·17)	0·59 (0·19)	0·59 (0·08)	1·26 (0·25)	1·10 (0·55)	2·02 (0·02)
Total	98·16	98·20	99·85	99·30	98·36	101·19	98·22
Si	1·890 (0·029)	1·890 (0·034)	1·910 (0·058)	1·980 (0·008)	1·940 (0·020)	1·910 (0·033)	1·910 (0·007)
Al	0·187 (0·069)	0·258 (0·048)	0·135 (0·077)	0·058 (0·024)	0·092 (0·034)	0·193 (0·062)	0·149 (0·006)
Fe^{2+}	0·224 (0·010)	0·112 (0·012)	0·215 (0·044)	0·123 (0·032)	0·132 (0·044)	0·184 (0·031)	0·155 (0·006)
Mg	0·960 (0·081)	0·981 (0·017)	1·040 (0·105)	1·100 (0·032)	0·970 (0·046)	1·020 (0·060)	1·030 (0·018)
Ca	0·724 (0·092)	0·712 (0·027)	0·700 (0·143)	0·718 (0·098)	0·821 (0·078)	0·658 (0·055)	0·696 (0·043)
Na	0·049 (0·009)	0·054 (0·012)	0·042 (0·015)	0·041 (0·006)	0·091 (0·019)	0·077 (0·037)	0·145 (0·010)
X_{Mg}	0·81 (0·01)	0·90 (0·01)	0·83 (0·03)	0·90 (0·02)	0·87 (0·02)	0·85 (0·02)	0·87 (0·00)

Run:	Px3	Lz3	Lz2	Lz5	Lz7	Lz10	Lz9
P (GPa):	5·2	2·6	3·0	6·0	6·0	6·5	6·5
T (°C):	680	700	750	680	750	650	700
SiO_2	53·89 (1·98)	54·84 (5·64)	54·23 (3·73)	55·33 (0·66)	55·31 (1·10)	53·41 (0·64)	55·20 (1·92)
Al_2O_3	4·95 (0·66)	1·17 (1·11)	0·70 (0·12)	1·06 (0·35)	1·57 (0·19)	2·87 (1·62)	0·28 (0·07)
FeO	5·06 (0·68)	3·27 (0·15)	3·15 (0·30)	4·22 (0·39)	3·84 (0·13)	3·78 (0·76)	2·02 (0·21)
MgO	18·28 (2·50)	23·41 (1·10)	21·69 (1·23)	30·11 (3·14)	27·30 (1·60)	26·45 (3·39)	17·64 (2·50)
CaO	15·07 (2·14)	15·36 (4·57)	18·08 (3·39)	7·75 (3·33)	13·75 (1·57)	11·46 (2·47)	23·57 (0·72)
Na_2O	1·75 (0·15)	0·24 (0·08)	0·24 (0·09)	0·39 (0·18)	0·22 (0·13)	0·81 (0·29)	0·04 (0·04)
Total	99·00	98·29	98·09	98·86	101·99	98·78	98·75
Si	1·950 (0·017)	1·980 (0·061)	1·980 (0·009)	1·960 (0·008)	1·930 (0·034)	1·910 (0·074)	2·020 (0·044)
Al	0·211 (0·034)	0·050 (0·058)	0·030 (0·004)	0·044 (0·015)	0·065 (0·008)	0·121 (0·068)	0·012 (0·003)
Fe^{2+}	0·153 (0·019)	0·099 (0·011)	0·096 (0·013)	0·125 (0·011)	0·112 (0·004)	0·113 (0·021)	0·062 (0·005)
Mg	0·986 (0·108)	1·260 (0·174)	1·180 (0·103)	1·590 (0·155)	1·420 (0·086)	1·410 (0·161)	0·962 (0·120)
Ca	0·584 (0·100)	0·594 (0·146)	0·707 (0·108)	0·294 (0·128)	0·514 (0·056)	0·439 (0·107)	0·924 (0·039)
Na	0·123 (0·010)	0·017 (0·005)	0·017 (0·007)	0·027 (0·013)	0·015 (0·008)	0·057 (0·023)	0·003 (0·003)
X_{Mg}	0·87 (0·02)	0·93 (0·01)	0·92 (0·00)	0·93 (0·00)	0·93 (0·00)	0·93 (0·01)	0·94 (0·00)

$X_{Mg} = Mg/(Mg + FeO^{tot})$.

calibrations. Data are compared with previous experimental results in ultramafic systems by considering chemical analyses of phases obtained at the lowest temperatures available, and at comparable pressures and compositions, specifically: (1) experiments performed on an Hawaiian pyrolite at 2·0–3·5 GPa, 1050–1100°C (Taylor, 1998); (2) experiments performed on a MORB pyrolite at 2·5–3·2 GPa, 925–1000°C (Niida & Green, 1999); (3) experimental data reported for a garnet lherzolite at 2·8–5·0 GPa, 900–1000°C (Brey *et al.*, 1990).

It is widely known that both experimentally produced and natural garnet peridotite minerals incorporate significant contents of Fe^{3+}. As a result, thermometers based on Fe–Mg exchange may be biased by uncertainties in Fe^{3+}/Fe^{tot} estimates, and the temperatures obtained will be inaccurate, particularly for mineral pairs such as garnet–clinopyroxene. For the sake of simplicity, given the high uncertainties in assessing the Fe^{3+}/Fe^{tot} ratios of mineral phases based on electron microprobe analyses, and the ultramafic nature of the bulk-rock

Table 6: WDS chemical compositions of garnets

Run:	Px8	Px7	Px6	Px2	Px5	Px3	Lz5	Lz7	Lz10	Lz9
P (GPa):	2·0	3·0	4·2	4·6	4·8	5·2	6·0	6·0	6·5	6·5
T (°C):	800	800	680	750	680	680	680	750	650	700
SiO_2	40·85 (0·50)	40·52 (1·39)	40·40 (0·02)	41·86 (0·53)	40·60 (0·37)	41·32 (0·60)	41·47 (1·10)	42·51 (1·07)	41·87 (0·55)	40·86 (2·15)
Al_2O_3	23·34 (0·47)	22·58 (0·15)	22·31 (1·50)	22·42 (0·29)	22·42 (0·22)	22·44 (0·62)	21·58 (1·04)	22·24 (1·07)	23·18 (1·50)	22·54 (1·07)
FeO	13·44 (0·77)	12·42 (2·85)	15·35 (0·01)	15·80 (2·40)	15·17 (1·15)	17·08 (2·25)	11·52 (1·02)	10·39 (2·03)	13·36 (0·26)	11·49 (1·39)
MgO	15·10 (0·83)	16·39 (0·61)	14·43 (0·35)	15·11 (0·93)	15·39 (0·46)	14·42 (0·96)	18·18 (0·67)	18·25 (1·72)	14·23 (0·85)	16·91 (0·63)
CaO	8·49 (0·92)	6·50 (0·04)	7·84 (0·28)	6·59 (0·34)	7·74 (0·94)	6·25 (0·47)	6·52 (0·98)	8·16 (1·59)	8·70 (0·74)	6·29 (1·98)
Na_2O	0·02 (0·02)	0·06 (0·01)	0·11 (0·06)	0·04 (0·04)	0·12 (0·09)	0·04 (0·03)	0·03 (0·01)	0·00 (0·00)	0·01 (0·02)	0·00 (0·00)
Total	101·54	98·65	100·80	101·99	101·95	101·74	99·61	101·82	101·38	98·20
Si	2·939 (0·021)	2·976 (0·077)	2·953 (0·053)	3·015 (0·050)	2·928 (0·035)	2·999 (0·056)	2·999 (0·035)	3·000 (0·055)	3·021 (0·055)	3·000 (0·033)
Al	1·979 (0·031)	1·922 (0·029)	1·922 (0·095)	1·903 (0·012)	1·905 (0·016)	1·919 (0·040)	1·839 (0·077)	1·850 (0·082)	1·971 (0·079)	1·950 (0·078)
Fe^{2+}	0·809 (0·044)	0·938 (0·170)	0·938 (0·014)	0·952 (0·145)	0·915 (0·070)	1·037 (0·137)	0·697 (0·066)	0·613 (0·117)	0·806 (0·036)	0·705 (0·083)
Mg	1·619 (0·084)	1·794 (0·082)	1·572 (0·066)	1·622 (0·092)	1·654 (0·049)	1·560 (0·103)	1·960 (0·067)	1·920 (0·175)	1·530 (0·067)	1·850 (0·059)
Ca	0·654 (0·071)	0·512 (0·007)	0·614 (0·011)	0·509 (0·026)	0·598 (0·070)	0·486 (0·041)	0·505 (0·066)	0·617 (0·124)	0·673 (0·067)	0·495 (0·142)
Na	0·003 (0·004)	0·009 (0·002)	0·016 (0·008)	0·006 (0·005)	0·017 (0·013)	0·006 (0·004)	0·004 (0·002)	0·000 (0·000)	0·001 (0·002)	0·000 (0·001)
X_{Mg}	0·67 (0·02)	0·70 (0·02)	0·63 (0·01)	0·63 (0·03)	0·64 (0·01)	0·60 (0·04)	0·74 (0·01)	0·76 (0·03)	0·65 (0·02)	0·72 (0·01)
X_{Ca}	0·21 (0·02)	0·17 (0·01)	0·20 (0·01)	0·16 (0·01)	0·19 (0·03)	0·16 (0·01)	0·16 (0·02)	0·20 (0·04)	0·22 (0·02)	0·16 (0·05)

$X_{Mg} = Mg/(Mg + Fe^{tot})$; $X_{Ca} = Ca/(Mg + Fe^{2+} + Ca)$.

Table 7: WDS chemical compositions of amphiboles

Run:	Px8	Px9	Px11	Lz1	Lz4
P (GPa):	2·0	2·2	2·4	2·2	2·4
T (°C):	800	700	700	700	700
SiO_2	47·10 (0·75)	51·41 (0·83)	46·32 (2·07)	42·67 (2·68)	43·12 (2·92)
Al_2O_3	12·51 (0·64)	6·22 (1·00)	12·82 (1·84)	2·67 (0·16)	3·91 (0·20)
FeO	5·73 (0·21)	7·49 (0·32)	5·61 (0·63)	2·98 (0·09)	2·89 (0·28)
MgO	19·49 (0·78)	21·03 (0·98)	18·76 (1·44)	19·02 (1·09)	19·57 (1·46)
CaO	11·41 (0·57)	10·67 (0·79)	11·01 (1·15)	7·66 (0·73)	7·32 (0·60)
Na_2O	2·33 (0·27)	1·85 (0·12)	1·39 (0·17)	0·44 (0·06)	0·53 (0·05)
Total	98·56	98·68	95·91	75·44	77·35
Si	6·580 (0·092)	7·181 (0·165)	6·613 (0·178)	7·576 (0·077)	7·452 (0·050)
Al	2·060 (0·103)	1·024 (0·138)	2·157 (0·284)	0·559 (0·056)	0·796 (0·034)
Fe^{2+}	0·669 (0·027)	0·875 (0·023)	0·670 (0·066)	0·443 (0·024)	0·418 (0·036)
Mg	4·058 (0·117)	4·379 (0·116)	3·992 (0·245)	5·034 (0·090)	5·041 (0·068)
Ca	1·708 (0·090)	1·597 (0·122)	1·684 (0·159)	1·457 (0·078)	1·355 (0·048)
Na	0·631 (0·069)	0·501 (0·033)	0·385 (0·038)	0·152 (0·019)	0·178 (0·011)
X_{Mg}	0·86 (0·01)	0·83 (0·00)	0·86 (0·01)	0·92 (0·00)	0·92 (0·01)

$X_{Mg} = Mg/(Mg + Fe^{tot})$.

compositions, all Fe was treated as Fe^{2+} (Krogh-Ravna & Paquin, 2003).

As expected, Fe–Mg partitioning among coexisting phases suggests that magnesium preferentially partitions into olivine, clinopyroxene and orthopyroxene with respect to garnet. Mg–Fe partitioning between olivine and garnet is in agreement, within uncertainties, not only with previous experimental results, but also with curves calculated from the geothermometer of Brey & Köhler (1990) at pressure and temperature conditions representative for our experiments (Fig. 6a). Garnets always plot at lower X_{Mg} compared with previous experimental data, in agreement with the lower temperatures investigated in the present study.

Among the mineral pairs, olivine–orthopyroxene and olivine–clinopyroxene are the least sensitive to Mg–Fe partitioning with respect to temperature. Although the fractionations of iron and magnesium between olivine–orthopyroxene and olivine–clinopyroxene are unsuitable as geothermometers (Perkins & Vielzeuf, 1992; Taylor, 1998), our experimental data are in excellent agreement with the data of Brey *et al.* (1990), Taylor (1998) and Niida & Green (1999), plotting on a 1:1 trend, further suggesting that olivines, orthopyroxenes and clinopyroxenes approach equilibrium.

The Mg–Fe fractionation between garnet and clinopyroxene should be interpreted with more caution, because of the previously discussed uncertainties related to Fe^{3+}/Fe^{tot} ratios in garnets and clinopyroxenes. Our partitioning data have been compared with formulations by Krogh (1988) and Ai (1994) resulting in calculated temperatures, on average, 100–150°C higher than experimental temperatures. However, it is worth noting that even previous experimental data show a relatively dispersed distribution of Fe–Mg partitioning, resulting in uncertainties and inaccuracies of temperature estimates. Although Ai's geothermometer is based on a sufficiently large set of data for natural pyroxenites and peridotites, the effect of ferric iron on Mg–Fe partitioning between garnet and clinopyroxene might be responsible for such inaccuracy.

The pair garnet–orthopyroxene also gives values that are comparable with both previous experimental studies and calculated curves at comparable pressures and temperatures (Brey & Köhler, 1990). It is therefore suggested, on the basis of Mg–Fe partitioning data, that garnet–olivine and garnet–orthopyroxene appear to be at equilibrium.

Hydrous phases, i.e. amphibole, chlorite and the 10 Å phase, always show a preferential partitioning of Mg with respect to olivine (Fig. 6b and c). Nevertheless, data at temperatures up to 1100°C on amphibole–olivine pairs by Mysen & Boettcher (1975) and Niida & Green (1999) might indicate inversion of partitioning with rising temperature and, potentially, good sensitivity as a geothermometer.

Mass balance

Phase abundances have been estimated by least-squares mass-balance calculations. Inputs include average

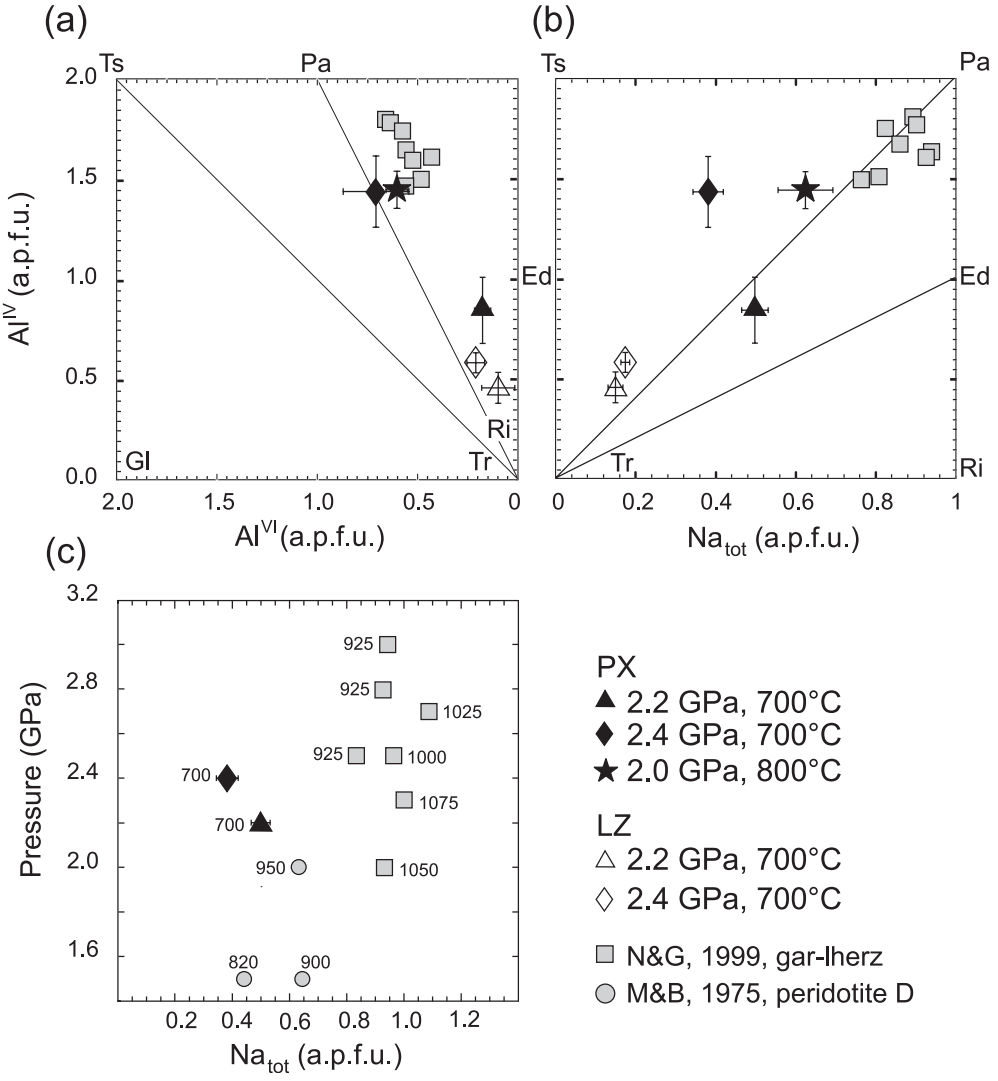

Fig. 4. Compositional variations in amphibole, atoms per formula unit (a.p.f.u.) calculated on the basis of 23 oxygens. (a) Tetrahedral (IV) vs octahedral (VI) aluminium; (b) tetrahedral aluminium vs total Na; (c) pressure–temperature dependence of Na in amphibole buffered by the presence of Na-clinopyroxene. Numbers represent temperature in °C. Grey squares, data from Niida & Green (1999); grey circles, data from Mysen & Boettcher (1975). Ts, tschermakite; Pa, pargasite; Ed, edenite; Ri, richterite; Tr, tremolite; Gl, glaucophane.

analyses and standard deviations for each phase in each experiment and bulk composition of the starting material. All iron has been treated as Fe^{2+}, as the ferric/ferrous ratio is unknown in the run charges; the H_2O component was not included in the calculations, as the H_2O content is not directly measured, but only evaluated indirectly by the abundance of hydrous phases. Propagated uncertainties are of the order of ±10–20% relative to the individual amounts determined.

Representative results are shown in Fig. 7, taking into account two different ranges of temperature: a relatively low-T section, between 680 and 700°C, for the olivine-poor lherzolite, and a section between 700 and 750°C for the Tinaquillo lherzolite composition. In the olivine-poor lherzolite, shaded bands represent reactions that lead to the transfer of H_2O component from amphibole, through chlorite to the 10 Å phase structure; in the Tinaquillo lherzolite composition, at higher temperature, reactions describe first H_2O transfer from amphibole- to chlorite-bearing assemblages, then complete dehydration.

It is worth noting that problems arose for experiments at 2·2 and 2·6 GPa, 700°C (runs Px9 and Px10, respectively). The fine-grained textures did not allow accurate analysis of olivine crystals. As a result, mass-balance calculations have been performed by assuming the olivine composition in an experiment at similar P–T conditions (i.e. run Px11, at 2·4 GPa, 700°C). Consequently, the olivine abundance obtained should be regarded with

Table 8: WDS chemical compositions of chlorites

Run:	Px9	Px10	Px6	Lz1	Lz4	Lz3	Lz2
P (GPa):	2·2	2·6	4·2	2·2	2·4	2·6	3·0
T (°C):	700	700	680	700	700	700	750
SiO_2	32·80 (1·24)	33·55 (0·55)	34·08 (0·92)	34·50 (1·13)	32·13 (3·48)	36·79 (1·57)	37·44 (3·50)
Al_2O_3	16·69 (0·46)	14·43 (0·41)	14·19 (1·48)	16·00 (0·92)	18·19 (2·67)	11·64 (1·45)	11·71 (1·35)
Fe_2O_3	0·41 (0·95)	0·81 (1·10)	0·93 (1·10)	0·19 (0·46)	1·06 (1·66)	0·00 (0·00)	0·00 (0·00)
FeO	7·50 (0·80)	8·59 (1·02)	4·22 (1·19)	2·84 (0·39)	2·23 (1·32)	3·63 (0·42)	3·96 (0·65)
MgO	30·89 (1·87)	30·40 (1·58)	33·02 (0·99)	34·18 (1·73)	33·86 (3·74)	35·35 (0·89)	35·36 (1·65)
CaO	0·24 (0·09)	0·36 (0·09)	0·58 (0·33)	0·13 (0·04)	0·19 (0·09)	0·08 (0·02)	0·17 (0·05)
Na_2O	0·07 (0·02)	0·04 (0·03)	0·32 (0·17)	0·08 (0·08)	0·03 (0·04)	0·00 (0·01)	0·01 (0·01)
Total	88·61	88·18	87·34	87·93	87·70	87·50	88·65
Si	6·220 (0·116)	6·450 (0·221)	6·460 (0·184)	6·440 (0·094)	6·010 (0·179)	6·920 (0·338)	6·970 (0·334)
Al	3·730 (0·069)	3·270 (0·072)	3·170 (0·289)	3·520 (0·219)	4·010 (0·315)	2·580 (0·301)	2·570 (0·405)
Fe^{3+}	0·058 (0·130)	0·117 (0·155)	0·133 (0·157)	0·027 (0·064)	0·149 (0·236)	0·000 (0·000)	0·000 (0·000)
Fe^{2+}	1·190 (0·137)	1·380 (0·187)	0·669 (0·186)	0·444 (0·066)	0·348 (0·206)	0·571 (0·072)	0·616 (0·073)
Mg	8·730 (0·180)	8·710 (0·277)	9·330 (0·246)	9·510 (0·255)	9·440 (0·344)	9·910 (0·127)	9·810 (0·126)
Ca	0·050 (0·021)	0·074 (0·018)	0·118 (0·070)	0·027 (0·009)	0·039 (0·027)	0·016 (0·003)	0·033 (0·010)
Na	0·027 (0·009)	0·013 (0·012)	0·116 (0·063)	0·028 (0·028)	0·012 (0·015)	0·001 (0·002)	0·004 (0·004)
X_{Mg}	0·87 (0·01)	0·85 (0·01)	0·92 (0·01)	0·95 (0·01)	0·95 (0·00)	0·95 (0·01)	0·94 (0·01)

$X_{Mg} = Mg/(Mg + Fe^{tot})$.

Table 9: WDS chemical compositions of the 10 Å phase structure recalculated on the basis of seven cations and 11 oxygens

Run:	Px5	Px3	Lz5	Lz10
P (GPa):	4·8	5·2	6·0	6·5
T (°C):	680	680	680	650
SiO_2	45·00 (0·52)	46·29 (1·37)	45·94 (1·28)	45·72 (1·48)
Al_2O_3	10·22 (0·81)	10·53 (0·68)	10·34 (0·54)	9·01 (0·79)
FeO	4·22 (0·35)	4·67 (0·53)	3·10 (0·36)	3·56 (0·58)
MgO	28·69 (0·38)	26·68 (1·18)	30·11 (0·89)	31·28 (1·36)
CaO	0·12 (0·03)	0·72 (0·35)	0·31 (0·16)	0·20 (0·19)
Na_2O	0·82 (0·05)	0·34 (0·26)	0·06 (0·04)	0·07 (0·02)
Total	89·07	89·23	89·87	89·83
Si	3·000 (0·035)	3·120 (0·061)	3·030 (0·044)	3·010 (0·090)
Al	0·803 (0·045)	0·836 (0·052)	0·804 (0·040)	0·699 (0·061)
Fe^{2+}	0·235 (0·014)	0·263 (0·030)	0·171 (0·020)	0·196 (0·031)
Mg	2·850 (0·029)	2·680 (0·069)	2·960 (0·053)	3·070 (0·118)
Ca	0·008 (0·002)	0·052 (0·025)	0·022 (0·012)	0·014 (0·014)
Na	0·106 (0·004)	0·044 (0·034)	0·008 (0·005)	0·008 (0·003)
X_{Mg}	0·92 (0·00)	0·91 (0·01)	0·95 (0·01)	0·94 (0·01)

$X_{Mg} = Mg/(Mg + Fe^{tot})$.

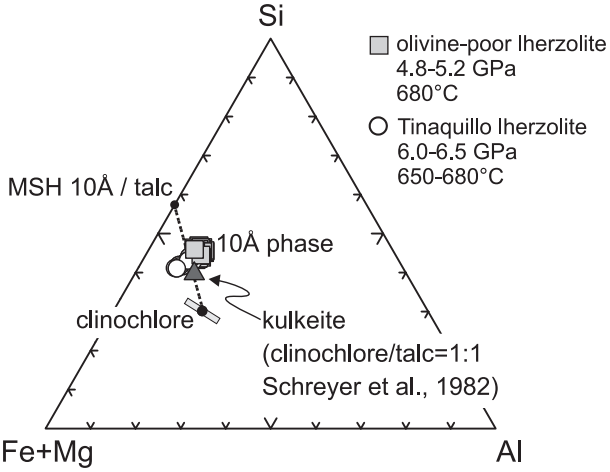

Fig. 5. Mineral chemistry of the 10 Å phase structure in the system (Fe + Mg)–Al–Si.

caution. At 2·4 GPa, 700°C chlorite was absent in the phase assemblage, whereas it appears at lower (2·2 GPa) and higher pressure (2·6 GPa). Whether this is a result of complex phase relationships involving amphibole solid solutions (see the section on amphibole breakdown reactions) is still unclear. However, it should be noted that chlorite abundance follows a similar trend in the

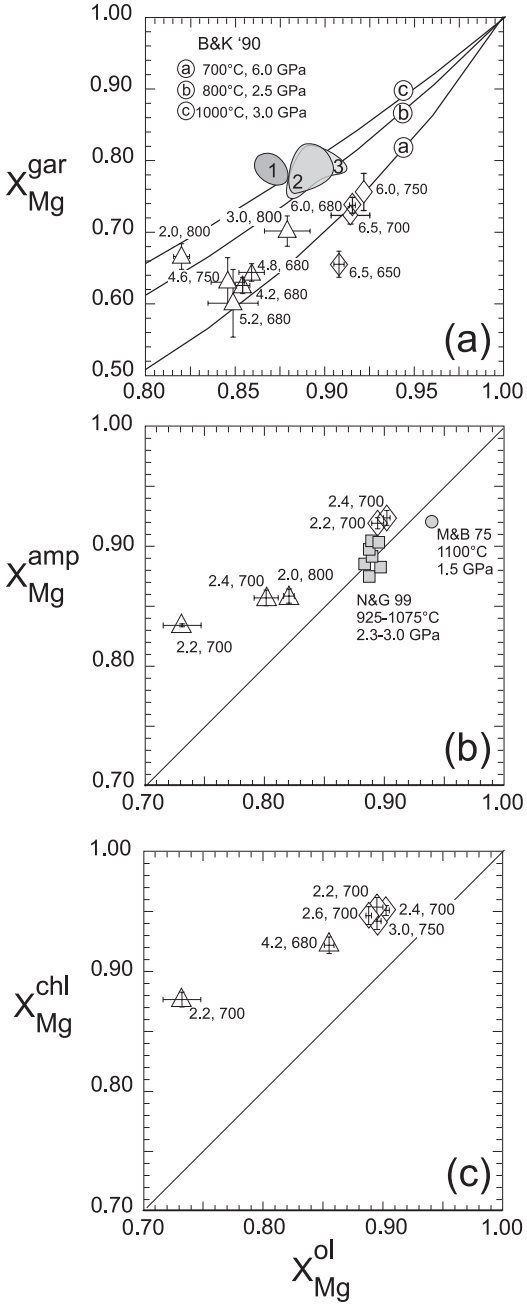

Fig. 6. (a) Fe–Mg partitioning of olivine vs garnet. $X_{Mg} = Mg/(Mg + Fe^{tot})$. Curves a, b and c are calculated from the Brey & Köhler (1990) geothermometer (B&K '90); grey fields represent previous experimental data from: (1) Taylor (1998) (1050–1100°C, 2·0–3·5 GPa; Hawaiian pyrolite, HPY 40); (2) Niida & Green (1999) (925–1000°C, 2·5–3·2 GPa, MORB pyrolite, MPY 40); (3) Brey *et al.* (1990) (900–1000°C, 2·8–5·0 GPa, garnet lherzolite, J4). (b) Fe–Mg partitioning of olivine vs amphibole. (c) Fe–Mg partitioning of olivine vs chlorite. Hydrates always show a preferential partitioning of Mg with respect to olivine. Open triangles, olivine-poor lherzolite composition; open diamonds, Tinaquillo lherzolite composition; grey circle, Mysen & Boettcher, (1975; M&B 75); grey squares, Niida & Green (1999; N&G 99). Numbers represent pressure in GPa, and temperature in °C, respectively. Error bars are based on the 1σ standard deviations given in Tables 3–9.

Tinaquillo lherzolite composition, suggesting effective complexities in topologies at such P–T conditions.

The olivine-poor lherzolite composition shows a lower abundance of olivine (<34 wt %), compared with the Tinaquillo lherzolite (ranging from 47 to 70 wt %), as expected based on the different Ca and Al contents in the starting materials. As a result, in the olivine-poor lherzolite the higher Ca and Al content maximize the abundance of clinopyroxene and garnet, whereas orthopyroxene occurs only at relatively high temperatures (800°C) and in anhydrous phase assemblages.

Mass-balance calculations provide useful information to identify the reactions responsible for variations in phase assemblages. In the pressure range 2·2–2·6 GPa, phase abundances suggest the reaction

$$\text{amphibole} + \text{olivine} \pm H_2O = \text{clinopyroxene} + \text{orthopyroxene} + \text{chlorite} \quad (2)$$

in the Tinaquillo lherzolite (with increasing pressure), and

$$\text{amphibole} = \text{clinopyroxene} + \text{chlorite} \pm \text{garnet} \quad (3)$$

in the olivine-poor lherzolite. As pressure increases, at T lower than 700°C, garnet increases and chlorite decreases up to 4·2 GPa. At higher pressure, phase abundances of anhydrous minerals remain almost constant, suggesting that the appearance of the 10 Å phase structure might be explained by a continuous reaction approaching

$$\text{chlorite} \pm \text{orthopyroxene} \pm \text{garnet} = 10\,\text{Å phase}. \quad (4)$$

Complexities in relationships between chlorite and the 10 Å phase will be discussed below.

At temperatures ranging from 700 to 750°C, and pressures between 2·5 and 4·5 GPa, phase abundances suggest the chlorite breakdown reaction

$$\text{chlorite} + \text{clinopyroxene} = \text{olivine} + \text{garnet}(\pm \text{orthopyroxene}) + H_2O. \quad (5)$$

Breakdown of the 10 Å phase is constrained both by mass-balance calculations and by phase abundances retrieved by Rietveld full profile refinement of X-ray powder diffraction data. Despite uncertainties in mineral compositions and in the 10 Å phase crystal structure, the consistency between mass-balance calculations and Rietveld modelling is remarkable: run Px3 at 5·8 GPa, 680°C is composed of 30 wt % olivine, 33 wt % clinopyroxene, 33 wt % garnet, 4 wt % 10 Å phase as estimated by Rietveld refinement, and 33 wt % olivine, 39 wt % clinopyroxene, 24 wt % garnet, 4 wt % 10 Å phase as estimated by mass balance. Discrepancies may be ascribed to the presence of seed relics and/or to heterogeneities in mineral compositions. Comparison

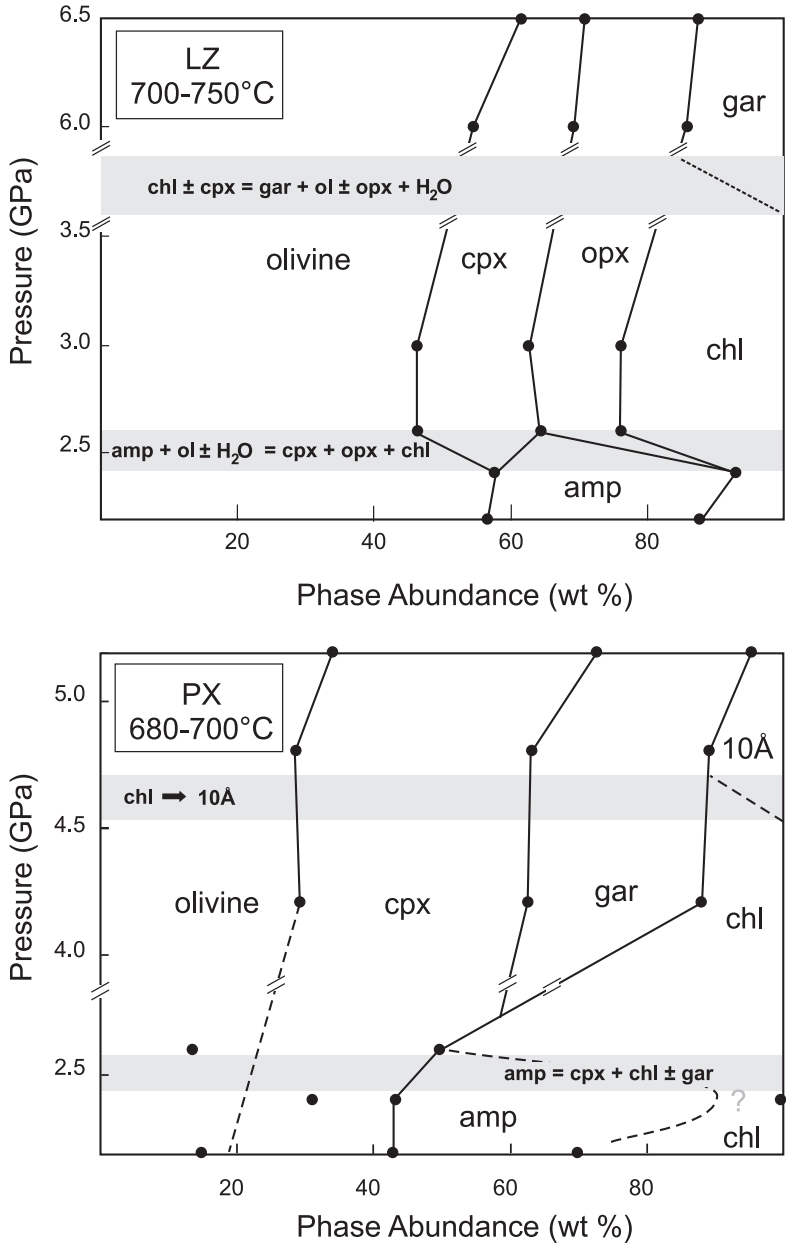

Fig. 7. Abundances of product phases calculated by mass balance as a function of pressure. The grey bands represent the pressure range in which the indicated reactions occur. Propagated uncertainties are of the order of 10–20% relative.

between phase proportions in Px3 and Px2 supports the breakdown reaction for the 10 Å phase

$$10\,\text{Å phase} + \text{clinopyroxene} = \text{garnet} + \text{orthopyroxene} + H_2O. \quad (6)$$

Amphibole breakdown reactions

Chemographic analysis further constrains the amphibole breakdown reaction at T lower than 700°C. In Fig. 8 phases are projected in the quaternary system $CaO–AlO_{3/2}–SiO_2–HO_{1/2}$ (CASH) from olivine and the exchange vectors $FeMg_{-1}$ and $NaAlCa_{-1}Mg_{-1}$, to account for Na substitution in both amphibole and clinopyroxene. Phase assemblages are deduced from experimentally determined phase assemblages and by the stability of solid solutions in the pressure range considered here.

The entire amphibole solid solution tremolite–pargasite is stable to 1·5 GPa (Jenkins, 1983). As pressure increases amphibole coexisting with clinopyroxene and

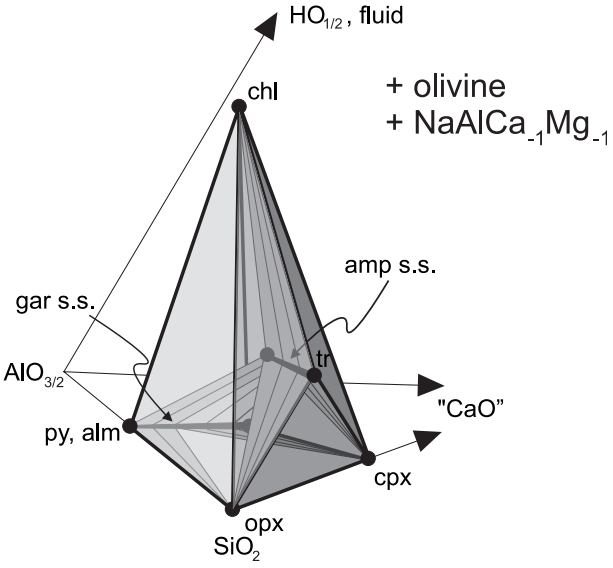

Fig. 8. Schematic chemographic relationships between amphibole, chlorite and anhydrous minerals within the tremolite pressure stability field projected from olivine and the exchange vectors $FeMg_{-1}$ and $NaAlCa_{-1}Mg_{-1}$. The amphibole solid solution range intersects the plane chlorite–orthopyroxene–clinopyroxene, which is, therefore, expected to be metastable as long as amphibole is stable.

chlorite progressively moves towards the join $AlO_{3/2}$–CaO. Amphibole at 2·2 GPa still lies above the geometric plane chlorite–orthopyroxene–clinopyroxene, whereas at 2·4 GPa its composition closely approaches this plane.

Compositionally, amphiboles stable at different pressures describe a join crossing the plane chlorite–orthopyroxene–clinopyroxene. This implies that the phase assemblage that defines such a plane is not stable when amphibole *sensu stricto* is stable and that complete solution occurs in Na–Ca amphiboles. Assuming that Na–Al-poor series (tremolite) destabilize first and pargasites at higher pressures, amphibole breakdown should be described by the degenerate reaction

$$\text{amphibole} + \text{olivine} = \text{orthopyroxene} + \text{clinopyroxene} + \text{chlorite}. \quad (2b)$$

Although reaction (2b) lies on the H_2O saturation plane, it does not involve fluid, i.e. is H_2O conservative. Further displacement of the amphibole composition toward more Al-rich composition may lead to the degenerate reaction observed in the olivine-poor lherzolite:

$$\text{amphibole} = \text{clinopyroxene} + \text{chlorite} + \text{garnet}. \quad (3b)$$

Phase assemblages actually suggest that the ultimate pressure breakdown of amphibole within the *P–T* stability field of chlorite might occur in a H_2O-undersaturated portion of the compositional space; for example, as observed for zoisite in the stability field of lawsonite in CASH (Poli & Schmidt, 1998).

The behaviour of chlorite at high pressure

Thermal stability

The breakdown of chlorite in the simple system MASH is controlled by reaction (1), in the garnet stability field. Previous experimental studies have suggested a steep, negative slope to ~3·0 GPa, which flattens at increasing pressure, defining a backbend (Staudigel & Schreyer, 1977; Fockenberg, 1995; Pawley, 2003). The thermal stability of chlorite + enstatite (Fig. 1) is located between 860 and 880°C at 2·5 GPa, between 820 and 840°C at 3·5 GPa, and at ~650°C at 5·0–5·5 GPa (Pawley, 2003).

In Fe-bearing systems reaction (1) becomes divariant, and Fe–Mg partitioning between chlorite and garnet is expected to affect the phase equilibrium. Although the coexistence of chlorite and garnet has been found in a single experiment (Px6, at 4·2 GPa, 680°C), the data suggest a preferential partitioning of Fe into garnet with respect to chlorite. Therefore, as observed, the thermal stability of chlorite is shifted towards lower temperatures, compared with phase equilibria in the simple system MASH. None the less, because of the significant amount of the grossular component in garnet, the actual location of the chlorite thermal breakdown reaction is also related to the participation of clinopyroxene along a degenerate reaction in the composition space $CaO–Al_2O_3–SiO_2$ projected from olivine and H_2O (Fig. 9):

$$\text{chlorite} + \text{clinopyroxene} = \text{olivine} + \text{garnet} + H_2O. \quad (5b)$$

Furthermore, least-squares modelling of reactions (5a) and (5b) in the composition space CFMASH reveals that orthopyroxene is a product phase rather than a reactant as in equation (1).

The schematic arrangement of reactions in Schreinemakers' bundle of Fig. 9 is also consistent with a 10 Å phase breakdown via reaction (6).

The fate of chlorite at high pressure: the role of the 10 Å phase and its relations with chlorite

The occurrence of an Al-bearing 10 Å phase structure, forming at the expense of chlorite at pressure >4·8 GPa, 680°C, opens up a new scenario, not only in the overall picture describing hydrate-bearing phase assemblages in ultramafics at high pressure, but also in the definition of reactions that lead to the disappearance of chlorite with pressure. To define possible relations between chlorite and the 10 Å phase structure obtained in this study, some considerations are required on the distinctive mineral chemistry of these phases.

It is worth recalling that compositional changes in chlorite are mainly due to the Tschermak exchange, $Al^{VI}_{-1}Mg^{VI}_{1}Al^{IV}_{-1}Si^{IV}_{1}$. Although the obvious stable state consists of a talc-like layer (2:1 layer) with a net charge of −1·0 and a brucite-like interlayer with a +1·0 charge,

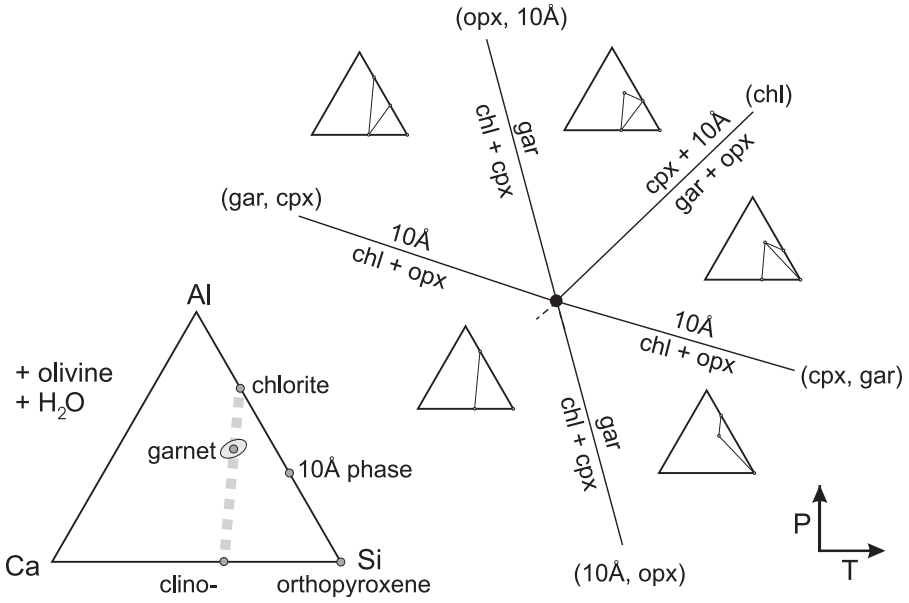

Fig. 9. Compositional degeneracy between clinopyroxene, garnet and chlorite in the model system CAS (Ca–Al–Si, atomic proportions) projected from olivine and water. The dotted line indicates the collinearity among chlorite, garnet and clinopyroxene, which suggests the degenerate reaction (5) (see text). Schreinemakers' bundle shows the arrangement of reactions involving chlorite in *P*–*T* space.

deviations are expected in the ordering of divalent vs trivalent cation substitutions in octahedral sites, resulting in difficulties in assessing whether the negative tetrahedral charge is totally compensated within the interlayer, or if a negative charge is also acquired within the octahedral sites of the talc-like layer (Bailey, 1988). As a result, the composition of the brucite interlayer is not easily determined. Furthermore, in low tetrahedral charge chlorites, vacancies in the 2:1 octahedral sites have been invoked to add and supply further negative charge (Rule & Bailey, 1988). The exchange vector responsible for such a substitution is the dioctahedral–trioctahedral substitution, $[]_1^{VI}Al_2^{VI}Mg_{-3}^{VI}$, which leads to the so-called di,trioctahedral chlorites (e.g. cookeite and sudoite). Dioctahedral chlorites, such as donbassite, exhibit further vacancies in the interlayer octahedral sites, as a result of the exchange vector $[]_1^{i}Si_2^{IV}Mg_{-1}^{i}Al_{-2}^{IV}$, where *i* denotes octahedral interlayer sites. With the exception of franklinfurnaceite, considered as an intermediate phase between brittle micas and chlorites, tri,dioctahedral chlorites, consisting of a trioctahedral 2:1 site, and dioctahedral interlayer are not known so far.

To evaluate the contribution of substitutions active in chlorites and in the 10 Å phase, experimental compositions obtained both in the olivine-poor lherzolite and in the Tinaquillo lherzolite are plotted in the ternary diagram talc, $Mg_3Si_4O_{10}(OH)_2$, amesite, $Mg_8Al_4{}^{VI}Si_4Al_4{}^{VI}O_{20}(OH)_{16}$, penninite, $Mg_{11}Al_1{}^{VI}Si_7Al_1{}^{VI}O_{20}(OH)_{16}$ (Fig. 10). It should be noted that, at the pressures considered in this study, the MSH 10 Å phase represents a stable phase (Fumagalli *et al.*, 2001) instead of talc. However, in the following discussions, as a result of the compositional analogies between these two phases, we will refer to a 'talc component'.

Chlorites, although dispersed, deviate from the join penninite–amesite along which the Tschermak substitution is active, suggesting that, together with a Tschermak substitution, an exchange vector pointing towards the talc composition might be envisaged. The talc component in chlorites might be described as a result of the vector $[]_1^{i}Si_2^{IV}Mg_{-1}^{i}Al_{-2}^{IV}$, if magnesium vacancies are expected or the vector $[]_1^{t}Si_3^{IV}Al_{-1}^{i}Al_{-3}^{IV}$, if aluminium vacancies are considered. In any case, although it is not rigorous, as the OH of the brucite layers are not considered here, clinochlore and talc might be related by the occurrence of vacancies in the interlayer, combined, so as to maintain charge balance, with Si,Al substitution within the tetrahedral sites. The overall result is a decrease of aluminium content, as observed in chlorites stable both in the olivine-poor lherzolite and in the Tinaquillo lherzolite at pressures up to 4·6 GPa.

On the other hand, looking at the 10 Å phase composition, it has been already observed in the mineral chemistry section that the Tschermak substitution is inconsistent with the mineral chemistry of this phase. Figure 10 further rules out the contribution of a Tschermak component, starting from an MSH 10 Å phase, to describe the mineral chemistry of the 10 Å phase structure obtained at pressures greater than 5·2 GPa. As a result, an alternative mechanism exists to take into account the ~0·8 a.p.f.u. of aluminium in the 10 Å phase structure.

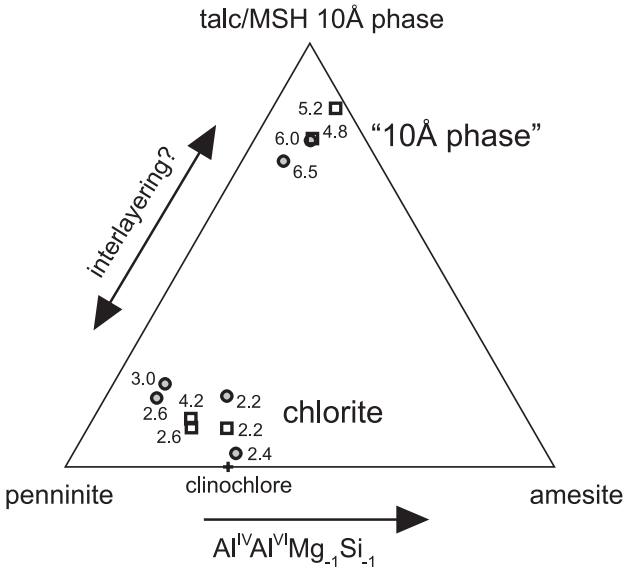

Fig. 10. Ternary diagram talc $[Mg_3Si_4O_{10}(OH)_2]$–amesite $(Mg_8Al_4^{VI}Si_4Al_4^{IV}O_{20}(OH)_{16}]$–penninite$[Mg_{11}Al_1^{VI}Si_7Al_1^{IV}O_{20}(OH)_{16}]$, showing the contribution of the 'talc–10 Å phase component' to the chlorite mineral composition. Squares, products in the olivine-poor lherzolite composition; circles, products in the Tinaquillo lherzolite. Numbers represent pressure in GPa.

The observed trend in the aluminium content of chlorites might be considered as a valid starting point to discuss the 10 Å phase. Aluminium in chlorite decreases with increasing pressure to a minimum limit, below which the chlorite structure is no longer stable. A minimum aluminium content requirement is also in agreement with the minimum interlayer charge on the brucite-type layer (Nelson & Roy, 1958), used to explain the unfeasibility of synthesizing low-Al chlorite. The decrease of aluminium might be combined with a pressure-dependent increase of interlayer vacancies, in accord with the exchange vector $[]_1^i Si_2^{IV} Mg_{-1}^i Al_{-2}^{IV}$ or $[]_1^i Si_3^{IV} Al_{-1}^i Al_{-3}^{IV}$ ('talc component'). As a result, the brucite interlayer might be totally 'removed' and hydroxyls might be expected to form water molecules in the interlayer. Such a substitution, if not completely accomplished, leads to compositions that are intermediate between talc with water in excess (MSH 10 Å phase) and chlorite, with the 'talc component' increasing as the reaction occurs.

It is worth noting that a simple intergrowth of two phases (chlorite and MSH 10 Å phase), as a result of preferential nucleation of MSH 10 Å on clinochlore seeds in the starting materials, might be envisaged at first sight; however, the homogeneity at the macroscopic

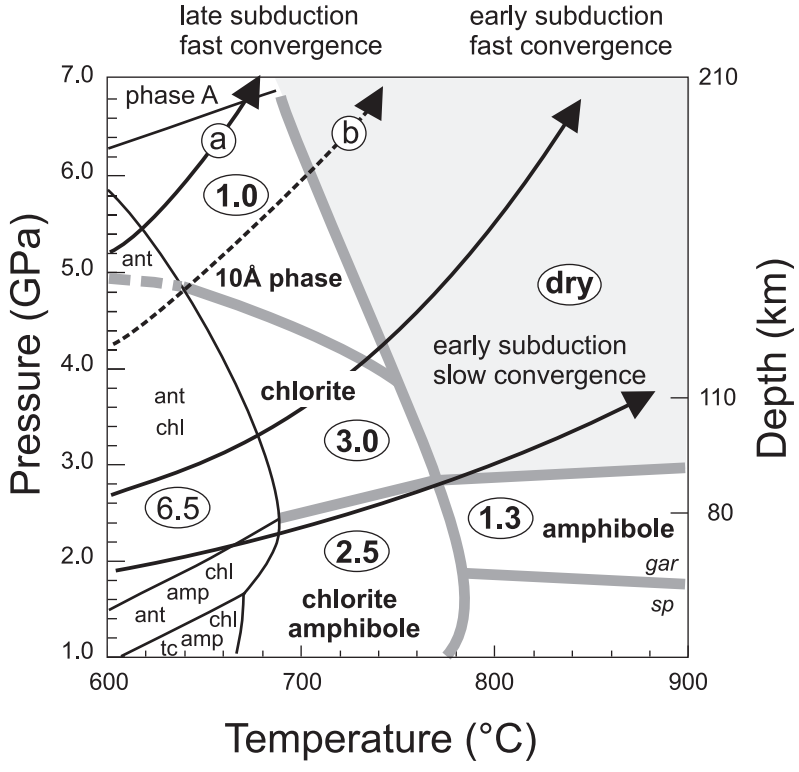

Fig. 11. Maximum *P–T* stability for hydrous phases in a fluid-saturated lherzolite composition compared with typical *P–T* paths of a subducting slab with a thin oceanic crust [continuous lines from Kincaid & Sacks (1997)]. Paths a and b refer to the *P–T* conditions for which the sketches of Fig. 13a and b are drawn, respectively; path a implies H_2O transfer from the 10 Å phase to phase A, whereas path b implies the ultimate devolatilization at the 10 Å phase breakdown. Numbers in ellipses show the amount of H_2O bound to hydrous phases and depict the dehydration history of the slab.

scale (scanning electron microscope images) and the lack of unequivocal chlorite diffractions in the X-ray pattern, do not corroborate such a hypothesis.

Whether such a 'talc substitution' is operating in the overall chlorite structure or is restricted to few domains is not deducible on the basis of mineral chemistry. Although transmission electron microscopy investigations are required, the compositional coincidence of the 10 Å phase structure with kulkeite (Fig. 5) allows us to describe the 10 Å phase structure as a mixed layered structure forming as a consequence of chlorite structural rearrangements, via 'talc substitution'. Indeed, although at the microprobe scale the aluminium content in the 10 Å phase structure appears to be homogeneously distributed, at the unit-cell scale Al-bearing domains of clinochlore composition might be 'mixed' with Al-free domains of talc composition, that is, at such high pressure conditions, domains of an MSH 10 Å phase composition.

In summary, a mixed-layered structure is a good candidate to explain the crystal chemistry and phase relationships of chlorite and the 10 Å phase. The compositional coincidence of the 10 Å phase structure and the mixed layered silicate kulkeite, along the exchange vector pointing to a 'talc–MSH 10 Å phase' component, might be explained by a pressure-dependent structural rearrangement of clinochlore.

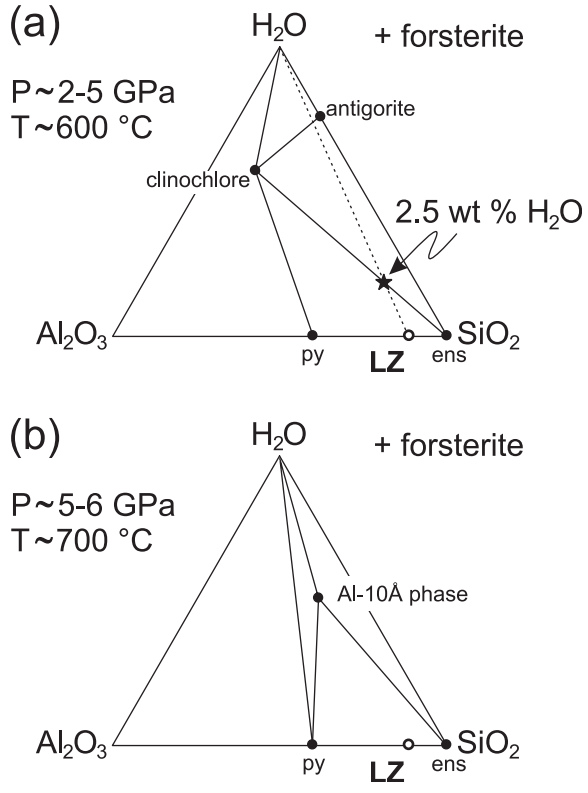

Fig. 12. Chemographic relationships in the model system Al_2O_3–SiO_2–H_2O projected from forsterite showing predicted phase assemblages at H_2O-undersaturated conditions, at $P \sim 2$–5 GPa, $T \sim 600$°C (a) and $P \sim 5$–6 GPa, $T \sim 700$°C (b). The dotted line represents lherzolite compositions with different H_2O content. The star located at the intersection between the dotted line and the tie-line clinochlore–enstatite corresponds to a lherzolite composition with 2·5 wt % H_2O. Antigorite is predicted to appear in this model system only at H_2O contents higher than 2·5 wt %. Py, pyrope; ens, enstatite.

GEODYNAMIC IMPLICATIONS

Constraints for the transport and release of water in subduction zones

To evaluate the dehydration history of the ultramafic portion of subducting slabs the experimentally defined phase diagram in Fig. 11 is compared with typical P–T paths described for slab surfaces (Kincaid & Sacks, 1997). Numbers represent the maximum H_2O content stored by hydrates in a Tinaquillo lherzolite composition, as evaluated by mass-balance calculations. Because of the relatively large uncertainties in phase proportions, especially for phase abundances lower than 15 wt %, H_2O contents should be considered as first-order estimates that largely depend on the bulk composition chosen and on the chemical composition of the mineral phases at the P–T conditions selected. As the H_2O content of the 10 Å phase structure remains unknown, the lower amount reported in literature for the MSH 10 Å phase (7·6 wt %, Wunder & Schreyer, 1992) was used. However, a mixed layered structure, as hypothesized in this study, would actually be able to incorporate a variable amount of water. As a consequence, numbers indicated in the region of stability of the 10 Å phase structure can be considered a lower limit for H_2O transport at depth.

Although the results presented here confirm that the major release of water in fluid-saturated systems is caused by the breakdown of antigorite (Ulmer & Trommsdorff, 1995, 1999), other hydrates still represent important reservoirs. Amphibole is restricted to relatively shallow depth, in the forearc region of a subduction zone. Most important is that any significant amphibole-related fluid release is feasible only at high temperature, as most low-temperature regimes would promote H_2O transfer to chlorite. Although it has been demonstrated that the depth of the slab surface below the volcanic front is unrelated to any simple geometrical relationship between the location of breakdown reactions in the slab and the location of the volcanic front (Poli & Schmidt, 2002; see Schmidt & Poli, 2003, fig. 9), it is worth noting that reactions involving chlorite–10 Å phase represent a critical step in the generation of fluids relevant for arc magmatism. Furthermore, in the coldest subduction environments the stability of a hydrous phase such as the 10 Å phase offers an explanation for the transfer of H_2O from antigorite–chlorite-bearing assemblages to

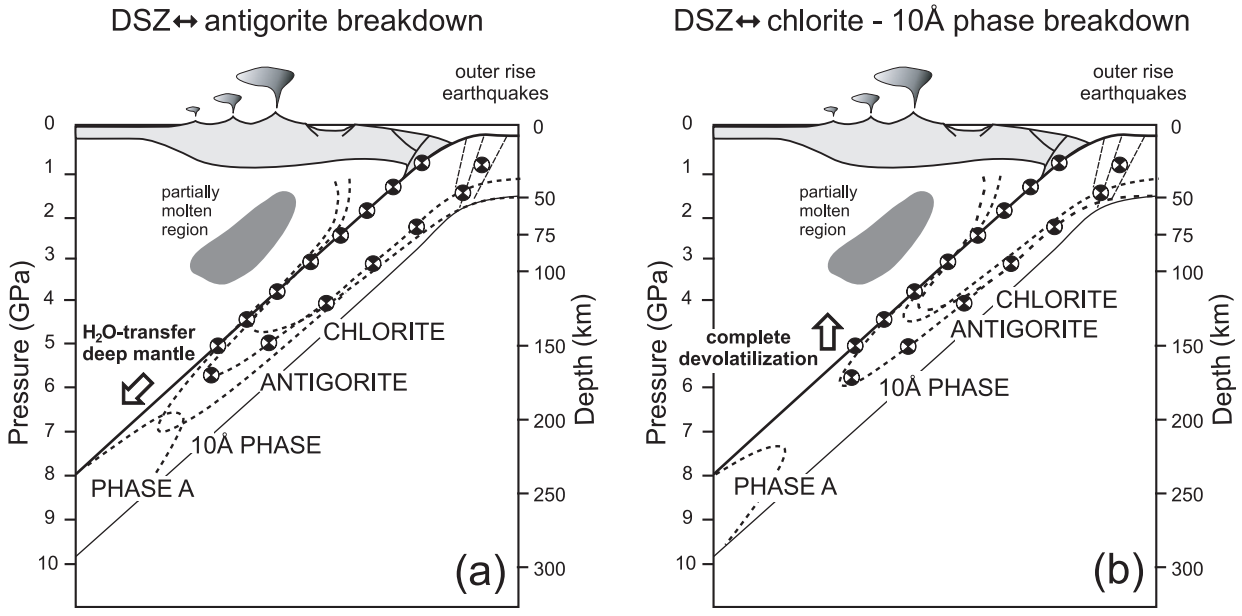

Fig. 13. Schematic illustrations showing the relationship between the thermal structure of a subduction zone, the stability field of hydrous phases in ultramafic rocks and the location of arc volcanism. Earthquake focal mechanisms (circles) have been used to indicate the location of the double seismic zone (DSZ) and not its kinematics. Dashed lines represent the stability field of hydrous phases as a function of P and T as given in Fig. 11. (a) If the lower plane of seismicity in the DSZ is attributed to antigorite breakdown (high H_2O contents and/or Al-poor bulk compositions), the thermal structure and phase diagrams support H_2O transfer to the deep mantle via dense hydrous magnesium silicates (DHMS) (left). (b) In contrast, if H_2O undersaturation and relatively Al-rich compositions prevail, the DSZ can be only related to the dehydration of the chlorite–10 Å phase breakdown and a hotter thermal structure is expected.

a phase A-bearing assemblage, therefore promoting volatile transport to the deepest upper mantle.

Chlorite–10 Å phase stability fields and double seismic zones in subducting slabs

Although harzburgites and depleted lherzolites are commonly expected to dominate in the uppermost oceanic mantle affected by hydrothermal metamorphism, the presence of enriched lherzolites in abyssal peridotites is the rule rather than the exception (Al_2O_3 >2 wt %, Niu *et al.*, 1997; Baker & Beckett, 1999; Constantin, 1999). Furthermore, the occurrence of pyroxenites in the MORB mantle source was recently evaluated to explain the distinctive isotopic characteristics of clinopyroxenes from MORB (Salters & Dick, 2002). As a consequence, we might reasonably expect that Al-rich phases such as amphibole, chlorite and Al-10 Å phase contribute significantly to the volatile budget in subduction zones, as well as to the geodynamic consequences of hydrous phase breakdown, e.g. triggering earthquakes via a process of dehydration embrittlement.

Subducted lithosphere is expected to be only partially hydrated (i.e. serpentinized), because an extensively hydrated slab would be extremely buoyant. This implies that H_2O undersaturation occurs and the breakdown of serpentine is not necessarily related to major fluid release. If enough aluminium is present (Fig. 12), H_2O can be mostly stored in chlorite or in a Al-10 Å phase and the actual dehydration of the slab will occur at the breakdown of such phases, which have a larger stability field than antigorite.

The likelihood of H_2O undersaturation is maximal when partial hydration is required to explain the presence of hydrous phases along the lower plane of double seismic zones (DSZ) (Fig. 13) at depths of the order of 30–70 km below the Benioff plane (Seno & Yamanaka, 1996; Peacock, 2001; Hacker *et al.*, 2003; Yamasaki & Seno, 2003). Outer rise earthquakes are supposed to reveal the existence of fault systems in the flexural zone at the onset of subduction, which might activate water migration to depths of 50–70 km by a mechanism of seismic (dilatancy) pumping (Sibson, 1981; Peacock, 2001). If any water is capable of reaching such depths, it is reasonable to expect a condition of extreme H_2O undersaturation, where the stable phase assemblages in Al-bearing systems are dominated, over a wide range of P–T conditions, by the presence of first chlorite and then the 10 Å phase.

Recent efforts in modelling the thermomechanical and petrological structure of subduction zones have emphasized the relevance of antigorite breakdown as a possible threshold for H_2O storage within the slab and therefore as a trigger for intermediate-depth earthquakes,

including earthquakes along the lower plane of double seismic zones. If this is the case, the experimentally determined phase relationships presented here would suggest that the thermal structure of the slab is likely to be path a in Fig. 11 and H_2O transfer to DHMS takes place (Fig. 13). In contrast, if H_2O undersaturation and lherzolitic compositions prevail in the slab, then lower plane earthquakes should be related to the breakdown of chlorite–10 Å phase as the first fluids pulse out of the slab. This second hypothesis necessarily implies a thermal field incompatible with a petrological link between antigorite–chlorite–10 Å phase and DHMS (see path b in Fig. 11), and complete devolatilization of ultramafic rocks is expected to occur where the upper and lower plane of the DSZ join at *c.* 150–200 km depth (Fig. 13).

ACKNOWLEDGEMENTS

The first version of the manuscript was prepared while P.F. was a post-doctoral fellow at the Department of Geological Sciences, University of Michigan, Ann Arbor. Many thanks go to L. Stixrude and C. Lithgow-Bertelloni for enlightening discussions. This experimental work has benefited greatly from the support of CNR-IDPA. We are most indebted to Max W. Schmidt for fruitful discussions on subduction-zone processes and for supporting microanalysis at Clermont-Ferrand. We thank David H. Green and Peter Ulmer for their thoughtful reviews. Financial support for this study was provided by COFIN and FIRST grants.

REFERENCES

Ai, Y. (1994). A revision of the garnet–clinopyroxene Fe^{2+}–Mg exchange geothermometer. *Contributions to Mineralogy and Petrology* **115**, 465–473.

Artioli, G., Fumagalli, P. & Poli, S. (1999). The crystal structure of $Mg_8Mg_2Al_2Al_8Si_{12}(O,OH)_{56}$ pumpellyite and its relevance in ultramafic systems at high pressure. *American Mineralogist* **84**, 1906–1914.

Bailey, S. W. (1988). Chlorites; structures and crystal chemistry. In: Bailey, S. W. (ed.) *Hydrous Phyllosilicates (Exclusive of Micas). Mineralogical Society of America, Reviews in Mineralogy* **19**, 347–403.

Baker, M. B. & Beckett, J. R. (1999). The origin of abyssal peridotites: a reinterpretation of constraints based on primary bulk compositions. *Earth and Planetary Science Letters* **171**, 49–61.

Bauer, J. F. & Sclar, C.B. (1981). The '10 Å phase' in the system MgO–SiO_2–H_2O. *American Mineralogist* **66**, 576–585.

Boillot, G., Girardeau, J. & Kornprobst, J. (1988). Rifting of the Galicia margin: crustal thinning and enplacement of mantle rocks on the seafloor. In: Boillot, G., Winterer, E. L., *et al.* (eds) *Proceedings of the Ocean Drilling Program, Scientific Results, 103*. College Station, TX: Ocean Drilling Program, pp. 741–756.

Brey, G. P. & Köhler, T. (1990). Geothermobarometry in four-phase lherzolites; II, New thermobarometers, and practical assessment of existing thermobarometers. *Journal of Petrology* **31**, 1353–1378.

Brey, G. P., Köhler, T. & Nickel, K. G. (1990). Geothermobarometry in four-phase lherzolites; I, Experimental results from 10 to 60 kbar. *Journal of Petrology* **31**, 1313–1352.

Bromiley, G. D. & Pawley, A. R. (2003). The stability of antigorite in the systems MgO–SiO_2–H_2O (MSH) and MgO–Al_2O_3–SiO_2–H_2O (MASH): the effect of Al^{3+} substitution on high-pressure stability. *American Mineralogist* **88**, 99–108.

Chinnery, N. J., Pawley, A. R. & Clark, S. M. (1999). *In situ* observation of the formation of 10 Å phase from talc + H_2O at mantle pressures and temperatures. *Science* **286**, 940–942.

Chou, I.-M. (1986). Permeability of precious metals to hydrogen at 2 kb total pressure and elevated temperatures. *American Journal of Science* **286**, 638–658.

Connolly, J. A. D. & Cesare, B. (1993). C–O–H–S fluid composition and oxygen fugacity in graphitic metapelites. *Journal of Metamorphic Geology* **11**, 379–388.

Constantin, M. (1999). Gabbroic intrusions and magmatic metasomatism in harzburgites from the Garrett transform fault: implications for the nature of the mantle–crust transition at fast-spreading ridges. *Contributions to Mineralogy and Petrology* **136**, 11–130.

Davies, J. H. & Stevenson, D. J. (1992). Physical model of source region of subduction zone volcanics. *Journal of Geophysical Research* **97**, 2037–2070.

Fockenberg, T. (1995). New experimental results up to 100 kbar in the system MgO–Al_2O_3–SiO_2–H_2O (MASH): preliminary stability fields of chlorite chloritoid staurolite MgMgAl-pumpellyite and pyrope. *Bochumer Geologische und Geotechnische Arbeiten* **44**, 39–44.

Frost, D. J. (1999). The stability of dense hydrous magnesium silicates in Earth's transition zone and lower mantle. In: Fei, Y.-W., Bertka, C. & Mysen, B. O. (eds) *Mantle Petrology: Field Observations and High Pressure Experimentation: a Tribute to Francis R. (Joe) Boyd. Geochemical Society, Special Publications* **6**, 283–296.

Frueh-Green, G. L., Plas, A. & Lécuyer, C. H. (1996). Petrologic and stable isotope constraints on hydrothermal alteration and serpentinization of the shallow mantle at Hess Deep (site 895). In: Mével, C., Gillis, K. M., Allan, J. F. & Meyer, P. S. (eds) *Proceedings of the Ocean Drilling Program, Scientific Results, 147*. College Station, TX: Ocean Drilling Program, pp. 255–291.

Fumagalli, P. & Poli, S. (1999). Phase relationships in hydrous peridotites at high pressure: preliminary results of multianvil experiments. *Periodico di Mineralogia* **68**, 275–286.

Fumagalli, P., Stixrude, L., Poli, S. & Snyder, D. (2001). The 10 Å phase: a high-pressure expandable sheet silicate stable during subduction of hydrated lithosphere. *Earth and Planetary Science Letters* **186**, 125–141.

Gasparik, T. (1987). Orthopyroxene thermobarometry in simple and complex systems. *Contributions to Mineralogy and Petrology* **96**, 357–370.

Green, D. H. (1963). Alumina content of enstatite in a Venezuelan high-temperature peridotite. *Geological Society of America Bulletin* **74**, 1397–1401.

Green, D. H. (1973). Experimental melting studies on a model upper mantle composition at high pressure under water-saturated and water-undersaturated conditions. *Earth and Planetary Science Letters* **19**, 37–53.

Hacker, B. R., Peacock, S. M., Abers, G. A. & Holloway, S. D. (2003). Subduction factory 2. Are intermediate-depth earthquakes in subducting slabs linked to metamorphic dehydration reactions? *Journal of Geophysiscal Research* **108**, 2030–2046.

Hamilton, D. L. & Henderson, C. M. B. (1968). The preparation of silicate composition by gelling method. *Mineralogical Magazine* **36**, 832–838.

Hebert, R., Bideau, D. & Hekinian, R. (1983). Ultramafic and mafic rocks from the Garrett Transform Fault near 13° 30′ S on the East

Pacific Rise: igneous petrology. *Earth and Planetary Science Letters* **65**, 107–125.

Hirschmann, M. M. & Stolper, E. M. (1996). A possible role for garnet pyroxenite in the origin of the 'garnet signature' in MORB. *Contributions to Mineralogy and Petrology* **124**, 185–208.

Jenkins, D. M. (1983). Stability and composition relations of calcic amphiboles in ultramafic rocks. *Contributions to Mineralogy and Petrology* **83**, 375–384.

Katayama, I., Parkinson, C. D., Okamoto, K., Nakajima, Y. & Maruyama, S. (2000). Supersilicic clinopyroxene and silica exsolution in UHPM eclogite and pelitic gneiss from the Kokchetav Massif, Kazakhstan. *American Mineralogist* **85**, 1368–1374.

Kawamoto, T., Hervig, R. L. & Holloway, J. R. (1996). Experimental evidence for a hydrous transition zone in the early Earth's mantle. *Earth and Planetary Science Letters* **143**, 587–592.

Kincaid, C. & Sacks, I. S. (1997). Thermal and dynamical evolution of the upper mantle in subduction zones. *Journal of Geophysical Research* **102**, 12295–12315.

Krogh, E. J. (1988). The garnet–clinopyroxene Fe–Mg geothermometer; a reinterpretation of existing experimental data. *Contributions to Mineralogy and Petrology* **99**, 44–48.

Krogh-Ravna, E. J. & Paquin, J. (2003). Thermobarometric methodologies applicable to eclogites and garnet ultrabasites. In: Carswell, D. A. & Compagnoni, R. (eds) *Ultrahigh Pressure Metamorphism. European Mineralogical Union Notes in Mineralogy* **5**, 229–253.

Leake, B. E., Woolley, A. R., Arps, C. E. S., *et al.* (1997). Nomenclature of amphiboles; report of the subcommittee on amphiboles of the International Mineralogical Association, Commission on New Minerals and Mineral. *Canadian Mineralogist* **35**, 219–246.

Luth, R. W., Virgo, D., Boyd, F. R. & Wood, B. J. (1990). Ferric iron in mantle-derived garnets; implications for thermobarometry and for the oxidation state of the mantle. *Contributions to Mineralogy and Petrology* **104**, 56–72.

Mengel, K. & Green, D. H. (1989). Stability of amphibole and phlogopite in metasomatized peridotite under water-saturated and water-undersaturated conditions. In: Ross, J. (ed.) *Kimberlites and Related Rocks. Geological Society of Australia, Special Publications* **14**, 571–581.

Milhollen, G. K., Irving, A. J. & Wyllie, P. J. (1974). Melting interval of peridotite with 5·7 per cent water to 30 kbar. *Journal of Geology* **82**, 575–587.

Muller, M. R., Robinson, C. J., Minshull, T. A., White, R. S. & Bickle, M. J. (1997). Thin crust beneath Ocean Drilling Program borehole 735B at the Southwest Indian Ridge. *Earth and Planetary Science Letters* **148**, 93–107.

Mysen, B. O. & Boettcher, A. L. (1975). Melting of a hydrous mantle: I. Phase relations of natural peridotite at high pressures and temperatures with controlled activities of water, carbon dioxide, and hydrogen. *Journal of Petrology* **16**, 520–548.

Nelson, B. W. & Roy, R. (1958). Synthesis of the chlorites and their structural and chemical constitution. *American Mineralogist* **43**, 707–725.

Niida, K. & Green, D. H. (1999). Stability and chemical composition of pargasitic amphibole in MORB pyrolite under upper mantle conditions. *Contributions to Mineralogy and Petrology* **135**, 18–40.

Niu, Y., Langmuir, C. H. & Kinzler, R. J. (1997). The origin of abyssal peridotites: a new perspective. *Earth and Planetary Science Letters* **152**, 251–265.

O'Neill, H. S. C. (1981). The transition between spinel lherzolite and garnet lherzolite, and its use as a geobarometer. *Contributions to Mineralogy and Petrology* **77**, 185–194.

Pawley, A. (2003). Chlorite stability in mantle peridotite: the reaction clinochlore plus enstatite = forsterite + pyrope + H_2O. *Contributions to Mineralogy and Petrology* **144**, 449–456.

Pawley, A. R. & Wood, B. J. (1995). The high-pressure stability of talc and 10 Å phase: potential storage sites for H_2O in subduction zones. *American Mineralogist* **80**, 998–1003.

Peacock, S. M. (2001). Are the lower planes of double seismic zones caused by serpentine dehydration in subducting oceanic mantle? *Geology* **29**, 299–302.

Perkins, D. & Vielzeuf, D. (1992). Experimental investigation of Fe–Mg distribution between olivine and clinopyroxene; implications for mixing properties of Fe–Mg in clinopyroxene and garnet–clinopyroxene thermometry. *American Mineralogist* **77**, 774–783.

Poli, S. & Schmidt, M. W. (1998). The high-pressure stability of zoisite and phase relationships of zoisite-bearing assemblages. *Contributions to Mineralogy and Petrology* **130**, 162–175.

Poli, S. & Schmidt, M. W. (2002). Petrology of subducted slabs. *Annual Review of Earth and Planetary Sciences* **30**, 207–235.

Rule, A. C. & Bailey, S. W. (1988). Refinement of the crystal structure of a monoclinic ferroan clinochlore. *Clays and Clay Minerals* **35**, 129–138.

Salters, V. J. M. & Dick, H. J. B. (2002). Mineralogy of the mid-ocean-ridge basalt source from neodymium isotopic composition of abyssal peridotites. *Nature* **418**, 68–71.

Schmidt, M. W. & Poli, S. (1998). Experimentally based water budgets for dehydrating slabs and consequences for arc magma generation. *Earth and Planetary Science Letters* **163**, 361–379.

Schmidt, M. W. & Poli, S. (2003). Generation of mobile components during oceanic crust subduction. In: Rudnick, R. L. (ed.) *Treatise on Geochemistry, Vol. 3: The Crust*. Amsterdam: Elsevier, pp. 567–591.

Schmidt, M. W. & Ulmer, P. (2004). A rocking multi-anvil: elimination of chemical segregation in fluid-saturated high pressure experiments. *Geochimica et Cosmochimica Acta* **68**, 1889–1899.

Schreyer, W., Medenbach, O., Abraham, K., Gebert, W. & Müller, W. F. (1982). Kulkeite a new metamorphic phyllosilicate mineral: ordered 1:1 chlorite/talc mixed-layer. *Contributions to Mineralogy and Petrology* **80**, 103–109.

Sclar, C. B., Carrison, L. C. & Schwartz, C. M. (1965). High-pressure synthesis and stability of a new hydronium-bearing layer silicate in the system MgO–SiO_2–H_2O. *Transactions of the American Geophysical Union* **46**, 184.

Seno, T. & Yamanaka, Y. (1996). Double seismic zones, compressional deep trench–outer rise events, and superplumes. In: Bebout, G. E., Scholl, D. W., Kirby, S. H. & Platt, J. P. (eds) *Subduction Top to Bottom. Geophysical Monograph, American Geophysical Union* **96**, 347–355.

Sibson, R. H. (1981). Controls on low-stress hydrofracture dilatancy in thrust, wrench, and normal fault terrains. *Nature* **289**, 655–667.

Smith, D. (1995). Chlorite-rich ultramafic reaction zones in Colorado Plateau xenoliths: recorders of sub-Moho hydration. *Contributions to Mineralogy and Petrology* **121**, 185–200.

Stalder, R. & Ulmer, P. (2001). Phase relations of a serpentine composition between 5 and 14 GPa: significance of clinohumite and phase E as water carriers into the transition zone. *Contributions to Mineralogy and Petrology* **140**, 670–679.

Staudigel, H. & Schreyer, W. (1977). The upper thermal stability of clinochlore, $Mg_5Al[AlSi_3O_{10}](OH)_8$, at 10–35 kb $P(H_2O)$. *Contributions to Mineralogy and Petrology* **61**, 187–198.

Susaki, J., Akaogi, M., Akimoto, S. & Shimomura, O. (1985). Garnet–perovskite transformation in $CaGeO_3$: *in situ* X-ray measurements using synchrotron radiation. *Geophysical Research Letters* **12**, 729–732.

Tatsumi, Y. & Eggins, S. (1995). Hoffman, P. F., Jeanloz, R. & Knoll, A. H. (eds) *Subduction Zone Magmatism*. Blackwell Science, Oxford, 211 pp.

Taylor, W. R. (1998). An experimental test of some geothermometer and geobarometer formulations for upper mantle peridotites with application to the thermobarometry of fertile lherzolite and garnet websterite. *Neues Jahrbuch für Mineralogie, Abhandlungen* **172**, 381–408.

Ulmer, P. & Trommsdorff, V. (1995). Serpentine stability to mantle depths and subduction-related magmatism. *Science* **268**, 858–861.

Ulmer, P. & Trommsdorff, V. (1999). Phase relations of hydrous mantle subducting to 300 km. In: Fei, Y.-W., Bertka, C. & Mysen, B. O. (eds) *Mantle Petrology: Field Observations and High Pressure Experimentation: a Tribute to Francis R. (Joe) Boyd. Geochemical Society, Special Publications* **6**, 259–281.

Wallace, M. E. & Green, D. H. (1991). The effect of bulk rock composition on the stability of amphibole in the upper mantle: implications for solidus positions and mantle metasomatism. *Mineralogy and Petrology* **44**, 1–19.

Woodland, A. B. & O'Neill, H. S. C. (1993). Synthesis and stability of $Fe^{2+}{}_3Fe^{3+}{}_2Si_3O_{12}$ garnet and phase relations with $Fe_3Al_2Si_3O_{12}$–$Fe^{2+}{}_3Fe^{3+}{}_2Si_3O_{12}$ solutions. *American Mineralogist* **78**, 1002–1015.

Woodland, A. B. & O'Neill, H. S. C. (1995). Phase relations between $Ca_3Fe^{3+}{}_2Si_3O_{12}$–$Fe^{2+}{}_3Fe^{3+}{}_2Si_3O_{12}$ garnet and $CaFeSi_2O_6$–$Fe_2Si_2O_6$ pyroxene solid solutions. *Contributions to Mineralogy and Petrology* **121**, 87–98.

Wunder, B. & Schreyer, W. (1992). Metastability of the 10 Å phase in the system MgO–SiO_2–H_2O (MSH). What about hydrous MSH phases in subduction zones? *Journal of Petrology* **33**, 877–889.

Wunder, B., Wirth, R. & Gottschalk, M. (2001). Antigorite: pressure and temperature dependence of polysomatism and water content. *European Journal of Mineralogy* **13**, 485–495.

Wyllie, P. J. (1988). Magma genesis, plate tectonics, and chemical differentiation of the Earth. *Review of Geophysics* **26**, 370–404.

Yamamoto, K. & Akimoto, S. I. (1977). The system MgO–SiO_2–H_2O at high pressures and temperatures—stability field for hydroxyl-chondrodite, hydroxyl-clinohumite and 10 Å phase. *American Journal of Science* **277**, 288–312.

Yamasaki, T. & Seno, T. (2003). Double seismic zone and dehydration embrittlement of the subducting slab. *Journal of Geophysical Research* **108**, 2212–2232.

Zhang, J., Li, B., Utsumi, W. & Liebermann, R. C. (1996). *In situ* X-ray observations on the coesite–stishovite transition: reversed phase boundary and kinetics. *Physics and Chemistry of Minerals* **23**, 1–10.